Journal of Materials Chemistry B

Bioelectronics with Nanocarbons

Journal:	*Journal of Materials Chemistry B*
Manuscript ID	TB-REV-06-2018-001600.R1
Article Type:	Review Article
Date Submitted by the Author:	07-Aug-2018
Complete List of Authors:	Rastogi, Sahil; Carnegie Mellon University College of Engineering, Department of Biomedical Engineering Kalmykov, Anna; Carnegie Mellon University College of Engineering, Department of Biomedical Engineering Johnson, Nicholas; Carnegie Mellon University College of Engineering, Department of Materials Science and Engineering Cohen-Karni, Itzhaq; Carnegie Mellon University College of Engineering, Department of Biomedical Engineering and Department of Materials Science and Engineering

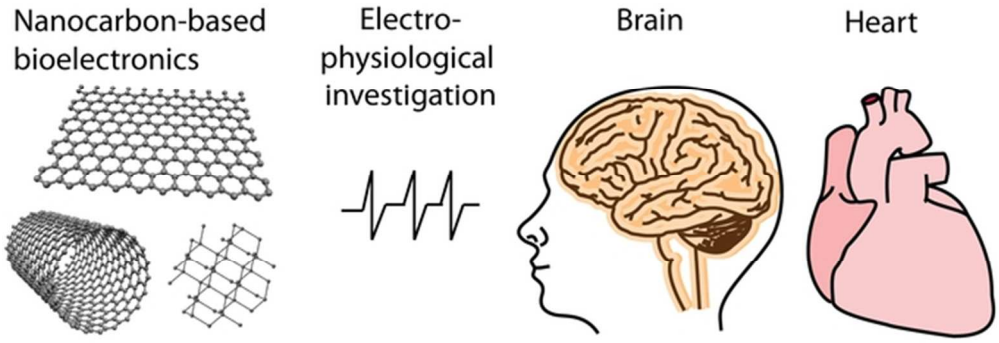

Smart bioelectronics fabricated from nanocarbons have the potential to enable seamless integration with electrogenic cells and tissues

57x24mm (300 x 300 DPI)

Bioelectronics with Nanocarbons

Sahil Kumar Rastogi,[1] Anna Kalmykov,[1] Nicholas Johnson,[2] Tzahi Cohen-Karni[1,2]

1 Department of Biomedical Engineering, Carnegie Mellon University, Pittsburgh, Pennsylvania, 15213, USA.

2 Department of Materials Science and Engineering, Carnegie Mellon University, Pittsburgh, Pennsylvania, 15213, USA.

INTRODUCTION

Excitable cells such as cardiomyocytes (CMs) and neurons interact with each other through electrical signals called action potentials, that occur due to the flow of certain ions across the cell membrane through ion-specific channels and pumps.[1, 2] Since the pioneering works in the 18th to 20th centuries that established a link between the electrical activity and cellular function,[3-5] generations of investigators have invested immense efforts into building and developing tools to study electrophysiology. Characterizing the electrical signals have enabled understanding of the intracellular processes and intercellular communications involved in the functioning of the heart and brain tissues. Investigating electrical signals is crucial to understand pathophysiology, since most cardiac and neurological disorders are linked to impaired electrical activity at the cellular and/or cellular network level.[6-8] In addition to fundamental research, pharmaceutical industries rely heavily on *in vitro* electrophysiological assay systems since the ion channels that are the basis of electrical activity serve as one of the major therapeutic drug targets.[9, 10]

Over the years, many modalities have been developed to monitor electrical activity at (i) macro-scale, i.e. at tissue scale, such as functional magnetic resonance imaging (fMRI),[11] positron emission tomography (PET), and electroencephalography (EEG), and (ii) high resolution nano/micro-scale, i.e. at a single-to-few cells level, such as patch clamp, microelectrode arrays (MEAs) and field effect transistors (FETs).[12]

Currently, MEAs and FETs (Figure 1) are gaining popularity because of their well-established microfabrication methods, consolidated transduction principle,[13] and the possibility to enable long-term and multi-site recordings at sub-msec temporal resolution.[14, 15] MEAs and FETs can be referred to as passive and active devices, respectively. When an excitable cell is interfaced with the electrode or the transistor, a cleft is formed which generates a resistance called seal resistance or R_{Seal}. Excitation of the cell leads to the flow of ions across the cell membrane. This gives rise to an extracellular potential difference, V_{extra} with respect to the bath solution. When the MEAs and FETs are interfaced with the cells, the V_{extra} leads to a change in the recorded potential in the case of MEA or change in the recorded current in the case of FET, thus enabling recording of the cellular electrical activity.[12]

A crucial element in any bioelectronic device is the sensing material interfaced with the biological system to record or modulate its electrical activity. Many efforts have been invested to address the size and mechanical mismatch between these systems.[16, 17] Another important aspect of bioelectronical devices is the compatibility of materials with the biological system since that can affect the long term stability of the devices, reliability of recordings, and pose health risks.[16, 17] The surface chemistry, presence of impurities and degradation of material over time play a role on both cell-sensor interface and adhesion, and host-tissue response such as inflammation and

cell death. Therefore, it is essential to investigate the effect of such materials on cells and tissues prior to exploring them for bioelectronics.

The scale and outstanding emergent physical and chemical properties make nanomaterials excellent candidates for highly sensitive, seamless integration with the biological system.[18, 19] Over the past several decades, a variety of carbon-based nanomaterials have emerged, as illustrated in Figure2. These nanocarbons exhibit a wide variety of structures, morphologies, and physical and chemical properties. The combination of high mechanical flexibility (in the case of carbon nanotubes and graphene), stability, and tunable electrical, physical and chemical properties by covalent and non-covalent functionalizations have made them popular in the field of bioelectronics. This review emphasizes recent advances in bioelectronics enabled by nanocarbons such as carbon nanotubes, nanocrystalline diamonds, graphene and its derivatives, i.e. planar graphene, porous graphene and out-of-plane grown three-dimensional (3D) graphene. We will briefly discuss the relevant synthesis and properties of these nanomaterials, and their effect on cells in terms of viability, adhesion and maturation, followed by their use in MEAs and FETs to record and stimulate CMs and neurons.

NANOCARBONS

Carbon Nanotubes

Carbon nanotubes (CNTs) are cylindrical nanostructures of seamless rolled-up sheets of graphene,[20] an atomic layer of two-dimensional (2D) honeycomb sp^2-hybridized carbon lattice. Single walled and multiwalled carbon nanotubes (SWNT and MWNT) are composed of one or more graphene layers, respectively.[20] They were first observed in 1952,[21] but more extensively characterized in 1991 and 1993.[22, 23] Structurally different types of SWNTs include zigzag,

armchair and chiral conformations.[20] Depending on the conformation, SWNTs can be either metallic, or semiconducting with tunable band-gap.[24]

CNTs have been explored in electronics due to their high thermal conductivity, low electron scattering, and controlled band-gap,[20] and as electrodes or electrode coatings due to their high surface area, conductivity, and wide electrochemical water window.[20, 25] High elastic modulus (1 TPa) and tensile strength (100 GPa) enables the use of CNTs in composites for load bearing applications that are light-weight, with high aspect ratio further improving their load bearing and electrical conductivity.[20] Additionally, CNTs' high aspect ratio and resulting increased adsorption makes them attractive in drug delivery.[26] These properties are reported for individual CNTs and show a decrease on macroscale if unorganized architectures of CNT composites, films or coatings are used.[20] However, the use of aligned CNT films, yarn or fibers as well as three-dimensional (3D) CNT microarchitectures may allow a more direct scale up of CNTs' unique properties.[20] In this section, we will be focusing on the use of CNTs and their derivatives in bioelectronics.

CNT Synthesis

CNTs can be obtained using several methods such as: arc discharge, organic bottom-up synthesis, laser ablation, and chemical vapor deposition (CVD).[27] Arc discharge method involves direct current or pulsed current arc discharges between two graphitic electrodes in gas atmosphere that results in MWCNTs with fewer defects, but lower purity.[27] SWNTs synthesis by this method requires a composite anode, containing graphite and transition metal catalyst.[27] Bottom-up organic synthesis of CNTs uses aromatic macrocycles as a template, joined through their end groups, which allows for precise chirality and diameter control but results in low volume of the product.[27] Laser ablation CNT synthesis involves focusing a laser beam on a

composite target of graphite and transition metal catalyst.[27] This method results in high product quality and purity, however, the scale up using this method is challenging.[27] CVD, which involves thermal decomposition of carbon precursor gases on metal catalyst (Fe, Co, Ni) at high temperatures, allows for scaled up production and preferential synthesis of metallic or semiconducting SWNT.[20, 27] It is the most common CNT synthesis method, but it may require annealing or chemical treatments to remove contaminants.[20]

The above mentioned synthesis methods result in a number of impurities, such as carbonaceous materials and metals, which can interfere with CNTs' desired properties.[27] For living matter use, CNTs need to be biocompatible.[28] Previous studies had showed that CNTs with highest carbonaceous material were most toxic to the cells.[29] CNTs can be purified post synthesis to remove the contaminants.[27] Post-synthesis purification may involve hot acid wash, filtration, and sonication in organic solvents.[27] As selective large-scale synthesis of CNTs remains challenging, post processing separation methods are needed for mixed yield products.[27] For example, separation based on CNT chirality and thus the electrical properties can be achieved via density gradient centrifugation.[20]

CNT Toxicity and Cell Interfaces

CNT toxicity is up to debate; the contradictory findings in different studies are mainly attributed to experimental differences.[30] Studies concluded that the biodistribution and accumulation of CNTs can be influenced by the route of exposure (e.g. dermal contact, or inhalation), period of exposure, dose, dimensions of CNT (size, length, aspect ratio), and their surface chemistry.[30, 31] Other factors, such as remaining catalytic metal content and dispersant chemistry may alter the toxicity profile.[30] Biodistribution pathways of CNTs may involve reticuloendothelial (RES) mediated uptake and distribution to internal organs, mainly liver,

spleen and kidney.[28, 30] Pulmonary toxicity of CNTs was shown to be dose dependent, with possibility of respiratory inflammation and granuloma formation at higher doses, but was shown to have no adverse effects at doses of 0.1mg/animal. Researchers also evaluated cardiac, dermal and gastrointestinal toxicity, showing a possibility of oxidative stress and inflammation in a dose-dependent manner.[30] Surface chemistry of CNTs plays an important role on the toxicity profile.[28, 30] Pristine CNTs are highly hydrophobic[26] and tend to aggregate, which was shown to cause toxicity.[28] In the presence of oxygen, pristine CNTs have been shown to cause DNA damage, cell cycle disruption, and impose oxidative stress on the cell.[28, 32] To reduce the toxicity, the hydrophobic nature of CNTs can be altered by functionalization of CNT sidewalls.[26, 28, 33] Side wall modification can be achieved by organic covalent functionalization, such as oxidation and substitution or addition reactions, or non-covalent surfactant adsorption of lipids, proteins/ peptides, or DNA.[26] Several studies showed functionalized nanotubes can show dose-dependent toxicity.[32] On the other hand, other studies claimed that covalently functionalized CNTs, CNTs non-covalently functionalized with Pluronic surfactant or poly ethylene glycol (PEG), and oxidized CNTs with adsorbed proteins exhibited little cytotoxicity, as evidenced by evaluating cell morphology, viability and proliferation.[28] Functionalization of CNTs with higher molecular weight branched PEG showed decreased RES-mediated uptake and showed almost complete CNT clearance and minimum toxicity in *in vivo* toxicology studies.[28]

The CNT surface dictates their cell interaction. Using CNT nanotopography combined with electrical conductivity, researchers have demonstrated the use of CNT scaffolds as smart material for electroactive cells, such as CMs[34, 35] and neurons.[25, 36, 37] An increase in branching and neurite outgrowth was demonstrated in neurons that were cultured on functionalized CNTs.[38-40] CNT substrates promoted increased electrical coupling, increased neuronal activity,

and enhanced synapse formation and dynamics, that were superior to both planar conductive surfaces and non-conductive surfaces with nanotopology.[36] Additionally, CNTs' nanotopographical features and positive surface charge promoted neuronal adhesion.[25] When segregated mouse spinal explants were co-cultured on 3D CNT mesh *in vitro*, the explants reconnected via neurite outgrowth, exhibiting transmission of electrical signals between slices.[37] For CMs, CNTs were shown to induce maturation, as was indicated by gene expression, increase in gap-junctions and cell-cell coupling resulting in more mature electrophysiology.[34, 35]

CNT-cell interactions did not exclusively use electrical properties of CNTs. Mechanical properties of CNTs, such as tensile strength, and flexibility, have been used in bone tissue engineering.[41] By varying the composition of CNT-polycaprolactone composite, scaffolding material stiffness can be tuned to physiological stiffness, which has been shown to induce proliferation of osteoblasts.[41]

CNT Bioelectronics

CNTs have been used for field potential recordings and electrical stimulation of electrogenic cells[25] due to their high mechanical flexibility, high surface area, good charge injection, and electrochemical properties.[42-44] For both applications electrodes must be conductive, have low impedance, high capacitance, and a biocompatible interface with the cells.[25] Electrical stimulation aims to deliver sufficient charge to trigger an action potential without negatively affecting the cells. Upon delivery of charge during stimulation, chemical reactions occur on the electrode surface. Those reactions can involve capacitive double layer charging and discharging without electron transfer, and faradaic irreversible oxidation or reduction reactions.[25] CNTs and CNT coated surfaces were shown to have an increased

capacitance, decreased impedance and a wide electrochemical window, which makes them safe for cell stimulation.[25, 44]

The application of lateral currents to SWNT-polymer layer-by-layer films with cultured model neuronal cell line (NG108-15)[45] and to films of purified SWCNTs with cultured hippocampal cells[46] have shown to induce fast Na^+ inward current, indicating successful stimulation.[45, 46] More precise neural electrical stimulation was demonstrated by a vertically aligned CNT pillar MEA.[43] The MEAs were synthesized by Fe-catalyzed low pressure CVD (LPCVD) on phosphorus-doped polysilicon conductive traces (Figure 3A I), yielding dense vertically aligned CNT pillars (Figure 3A II). The charge injection of 1-1.6 mC/cm^2 demonstrated by the CNT MEA was superior to Pt and iridium oxide of the same geometric area.[43] Repeated stimulation of embryonic rat hippocampal neurons cultured on these arrays induced cell response that was recorded by tracking intracellular Ca^{2+} changes by fluorescence (Figure 3A III), with each peak indicating one to several action potentials.[43]

Vertically aligned CNT (VACNT) arrays were also used for both stimulation and recording. MEAs were fabricated from Ni catalyzed CVD grown carbon nanofibers that self-align vertically, creating a protruding array in 3D.[47] These MEAs were co-cultured with hippocampal slices and penetrated deep into the tissue.[47] The vertically aligned carbon nanofiber arrays were able to stimulate and record spontaneous neural activity and stimulus evoked field potentials.[47] CNT-MEA with a 3D protruded geometry were also fabricated.[48, 49] These VACNTs were synthesized on glassy carbon and Pt electrodes using Fe/Al catalyzed low pressure plasma-enhanced CVD (PECVD).[48] To improve electrochemical characteristics of the Pt-VACNT electrode,[48] graphene was deposited as an interface layer.[49] The VACNT electrodes were used to record from rat bone marrow stem cells[48] and immortalized neuronal cell line.[49] Furthermore,

transparent graphene VACNT MEAs were synthesized and used for rodent neuronal recording upon optical stimulation.[50] The graphene VACNT hybrid electrodes demonstrated superior signal-to-noise ratio (SNR) due to increased vertical surface area resulting in better seal resistance.[50]

To increase the effective electrode area while keeping the footprint low, researchers synthesized highly dense entangled CNTs on titanium nitride (TiN) conductive traces to form island–like MEAs with 3D morphology (Figure 3B I, II).[44] Cortical neurons and glia cells were co-cultured with the CNT MEA islands, where CNT surface roughness promoted cell adhesion.[44] CNT MEAs sensed spontaneous electrical activity with a high SNR (Figure 3B III).[44] CNTs were also used as MEAs to record extracellular potentials from CMs.[51] The MEAs were defined by lithography and CNTs were synthesized using CVD to form 3D island-like electrodes. The CNT MEAs were used to record from chick embryo CMs, outperforming TiN and planar Au electrode controls in terms of SNR.[51]

The benefits of CNT electrochemical properties have also been utilized, when CNTs were used as a coating material for implantable neuronal recording and stimulation electrodes.[52] Sharpened metal electrodes coated with CNT by electrodeposition displayed increased charge transfer, decreased impedance and reduced noise compared to measurements obtained before coating. These electrodes activated neurons upon stimulation more efficiently compared to Au-coated controls.[52] Composite coatings such as polypyrrole-CNT and CNT-poly(3,4-ethylenedioxythiophene) (PEDOT) have also been used to achieve similar improvements, i.e., lower impedance, increased SNR and enhanced electrochemical properties.[25] Additionally, the deposition methods, such as drop coating or microcontact printing, have been proposed as alternative CNT electrode modification methods.[25]

To reduce the tissue-electrode mechanical mismatch, researchers created flexible CNT-based electrodes. Fully flexible arrays with all-carbon circuitry were generated by CVD grown MWNTs based on patterned Ni catalyst.[42] CNT patterns were peeled off using a polymeric support to generate all-carbon, flexible MEAs, used for recording and stimulation of embryonic chick retinas. The advantage of these all-carbon electrodes was shown in seamless integration of electrode to circuit.[42] Furthermore, the CNTs allowed for large surface area and capacitive charge injection, were inert and resistive to corrosion.[42] To improve CNT adhesion to the fully flexible electronics, CNTs have been synthesized directly on polyimide via direct Ni-catalyzed CVD growth.[53] These flexible CNTs MEAs were used for electrocorticogram (ECoG) recording on rat's surface of the motor cortex.[53] Nanotopography of CNT allowed reduced electrode area while keeping interface area high.[53] Recently, CNTs were used to fabricate flexible, stretchable and transparent MEAs, where web-like interconnected CNT structures, synthesized by floating catalyst CVD followed by solvent induced condensation, were deposited on polydimethylsiloxane (PDMS) thin films.[54] The thin-film CNT MEAs maintained good electrochemical properties and allowed for simultaneous optical stimulation, Ca^{2+} imaging and electrophysiology recording. Furthermore, these MEAs were tolerant of tissue mechanical deformations and were used for ECoG recording from mice upon optical stimulation.[54]

Individual unique properties of CNTs on nanoscale can be harnessed on the macroscale by combining aligned CNTs to form carbon nanotube fiber (CNTf).[55] CNTfs were fabricated from CNT solutions in super-acids, where they form CNT/acid charge transfer complexes and self-align to form a liquid crystal. CNTfs are extruded by wet spinning and coagulated to form lightweight fibers without affecting CNT's key properties, i.e., strength, stiffness, electrical and thermal conductivity.[56, 57] The use of shorter CNTs enhances CNTf's bending fatigue. Due to

these properties, researchers have used CNTfs for chronic neural recording and stimulation *in vivo*.[58] They improved on the traditional implantable electrodes due to CNTf's lower tissue contact impedance, electrochemical properties, increased sensitivity, and resistance to biofouling.[58] The ultra-flexibility of CNTf electrodes led to reduced mechanical mismatch between electrode and the tissue.[58] At the same time, it posed a challenge upon implantation at high depth due to CNTf buckling.[59] CNTf electrodes were surgically implanted into mouse brain using 100 μm polyimide shuttle, however, the use of the shuttle has been responsible for an increased zone of neurodegeneration.[58] To avoid this adverse effect, an improvement in delivery method was recently demonstrated.[59] A microfluidic device was used to deliver thin and flexible CNTf electrodes deep into the mouse brain (Figure 3C I, II).[59] These fluidic micro drivers exert a viscous drag force on CNTf keeping the fiber under tension, thus preventing buckling.[59] After implantation the microfluidic driver is retracted, leaving CNTf delivered at a specific location and depth without the stiffener induced damage (Figure 3C II).[59] CNTf electrodes were used to record spiking activity in rodents from different regions in the brain and correlate them to the EEG recording obtained from the screw located on the right frontal cortex (Figure 3C II, III).[59] Spiking activity varied with implantation depth. When the CNTf microelectrode was implanted at 4 mm depth, the recorded signal was not correlated to the cortical EEG signal, suggesting subcortical hippocampal recording (Figure 3C III).[59]

The high flexibility, large surface area, and electrochemical properties of CNTs allowed researchers to create flexible and 3D electrodes for cell interfaces. CNT coatings improved commercially available implantable arrays.[25] Furthermore, the CNT remarkable properties enhanced the performance of the formed CNTfs, which allowed for deeper tissue penetration with inert and biocompatible carbon based electrodes.[58, 59]

Nanocrystalline diamonds

The family of nanocrystalline diamonds (NCD) covers a range of materials best differentiated by grain size and properties. NCD typically refers to diamond films with grains smaller than 100 nm and ultra-nanocrystalline diamond (UNCD) refers to diamond films with grains under 10 nm and amorphous grain boundaries.[61] As grain size increases from UNCD to NCD, the properties become increasingly similar to single crystal diamond, thus thermal conductivity, Young's modulus, and optical transparency increase, while electrical conductivity decreases. UNCD is black, while NCD can have optical transparency of up to 80 percent in the visible spectrum.[60, 61] These changes in properties are largely because smaller grains result in more grain boundaries and higher surface area which then lead to higher concentrations of sp^2 bonds and hydrogen content.[60] NCD has been increasingly of interest for MEA bioelectrical-interfaces due to its chemical stability, high electrochemical sensitivity, wide water potential window, optical transparency, biocompatibility, low noise generation, and tunable electrical conductivity.[60-64] In this section, we will discuss the synthesis and biocompatibility of NCD, as well as summarize the studies that have demonstrated the use of NCD for electrical interfaces with excitable cells.

NCD Synthesis

The first successful low-pressure synthesis of diamond structures and subsequent advancements[65-67] initiated decades of research into NCD materials. A detailed description of the history and continued advancements of diamond synthesis is extensively covered in several review articles.[68-70] Effective diamond synthesis requires sufficiently dense nucleation, however, the nucleation density of diamond on typical substrates is low.[61] Thus, a nucleation enhancement step, such as substrate abrasion, bias enhanced nucleation, or the addition of carbides or

nanodiamond particles is required. UNCD exhibits a smaller grain structure due to re-nucleation during growth, while NCD is typically grown without re-nucleation.[61] The three general synthesis techniques for thin film diamond are hot filament CVD (HFCVD),[71-75] plasma-assisted CVD (PACVD) or microwave plasma CVD (MWCVD),[61, 71, 76-79] and DC plasma discharge CVD (DCCVD).[80-84] HFCVD uses a filament, typically tungsten or tantalum, positioned directly above the substrate and heated to ca. 2200˚C to decompose the carbon precursor gas, usually CH_4. This technique is relatively simple and cost-effective, however, it suffers from potential filament corrosion and contamination of diamond with filament material.[68, 70, 72] MWCVD utilizes microwave power channeled into the chamber through a dielectric window to dissociate and activate the carbon precursor gas. This method is typically more expensive but can use a broader range of gas mixtures and there is no form of contamination.[68, 70] DCCVD is the most common form of plasma jet CVD that is used for diamond synthesis. High gas flow rates pass through direct current discharge, which ionizes the particles before they expand into a second chamber and collide with the substrate at a high speed. While this technique produces much faster growth rates compared to previously mentioned techniques, it can only deposit on ca. 1 cm^2 and subjects the substrate to high thermal shock, which shatters many commonly used materials.[68, 70]

NCD Biocompatibility

The biocompatibility of undoped NCD has been examined by cell proliferation, cell viability, and protein absorption.[85, 86] It was shown that cellular adhesion of neurons to hydrogen and oxygen terminated diamond (HTD and OTD, respectively) without protein functionalization is poor. After functionalization with laminin and poly-D-lysine, chick ciliary ganglion neurons adhered to OTD and HTD.[87] Rat hippocampal neurons adhered to protein functionalized OTD

and preserved their synaptic activity and somatic Ca^{2+} current density.[87] Cell adhesion and growth in presence or absence of protein functionalization varied depending on the NCD and cell types used. The biocompatibility of CVD grown NCD was demonstrated using osteoblasts,[88, 89] fibroblasts,[90] neural stem cells,[91, 92] mesenchymal stem cells,[93] and embryonic cortical neurons.[94, 95] Retinal neurons were unable to grow on OTD, while glial cells could only grow on protein-coated, OTD.[96] Additionally, the effect of heavy boron doping and nanostructuring was investigated through synthesis of undoped and doped, planar and 3D CNT templated NCD. It was shown that boron doping had no effect on cell adhesion or proliferation, whereas 3D templated NCD increased cell viability.[97] Synthesis conditions can affect NCD physicochemical properties that may lead to a change in their cellular interactions. The effects of different synthesis methods on biocompatibility of NCD has not been examined. Biocompatibility studies of NCD have used both HFCVD[70, 86, 90] and MWCVD[91, 92, 96, 97] synthesized NCD. The effects of HFCVD contaminations[72] on cellular viability and functionality has not been studied to-date. DCCVD is not as commonly used for NCD synthesis due to the previously mentioned limitations, thus no studies have shown biocompatibility of DCCVD grown NCDs. Overall, studies have shown high biocompatibility of NCD.

NCD Bioelectronics

Nanodiamond microelectrodes have been investigated in depth for electrochemical behavior and biosensing due to their large potential water window and high electrochemical sensitivity.[98, 99] Boron-doped NCD (BNCD) has been used in electrochemical sensing for DNA,[100, 101] glucose,[102] dopamine,[103] and uric acid.[104] Recently, the use of NCD for bioelectrical interfaces has garnered much attention due to diamond's unique combination of properties.[105-111] Diamond has highly tunable electrical properties and high conductivity when doped with boron,

excellent stability, and has tunable optical transparency. Optical transparency can be utilized for the combination of optical and electrophysiological methods. However, electrical interfaces with NCD typically use boron-doped NCD, and as doping concentrations increase, the optical transparency decreases.[60]

HFCVD grown boron-doped diamond on 30 μm diameter tungsten microelectrodes was used for *in vitro* detection of electrical signals in the Aplysia californica buccal mass.[105] Recording and stimulation of single cells was achieved, as well as separately measured serotonin release with the same electrode following patch clamp stimulation. More work needs to be done to combine these two recording modalities. The fabrication of an *in vivo* device which recorded action potentials from A. californica with lower noise and higher SNR compared to stainless steel electrodes was also demonstrated.[110]

A few years later, 1 mm HTD electrodes were used to record electrical signals from GT1-7 neuronal cells.[111] The electrodes recorded fast spikes of few msec duration and long spikes lasting tens of msec. This is likely the effect of individual firing neurons and synchronized activity, respectively. Previously, Ca^{2+} fluorescence imaging through the HTD was shown,[87] demonstrating the potential use of NCD based MEAs for simultaneous optical and electrical recording. Concurrently, single-crystalline HTD solution gated field effect transistors (SGFET) were fabricated to record action potentials from HL-1 cells and HEK293 cells[109]. HL-1 cells were seeded on of a 4 x 4 array of SGFETs (Fig 4A I-II). HL1 recordings with high temporal resolution (Figure 4A III) exhibited a time offset across different FETs due to the propagation of the signal in the culture.. More controlled recordings were obtained using patch-clamp to depolarize the membrane of single HEK293 cells genetically modified to express potassium channels.[109]

BNCD MEAs with 64 electrodes and various passivation layers such as oxide-nitride-oxide (ONO), NCD, and SU8 were used for recording of cultured HL-1 cells electrical activity.[107] ONO and NCD insulations were more stable than SU8. The BNCD-based MEA recorded electrical signals comparable to Au electrodes. The use of undoped-NCD for passivation further improved signal detection four folds. Additionally, BNCD electrodes were able to withstand the mechanical forces imposed by contractile cells.[107]

3D diamond structures have also been demonstrated for neural interfacing.[108] 20 μm electrodes were fabricated by complete encapsulation of CNTs in two layers of BNCD (Figure 4B I,II). The 3D nanostructured BNCD was shown to reliably stimulate and detect burst activity and local field potentials down to 10 μV from mouse hindbrain-spinal cord preparations and hippocampal cells. The electrodes exhibited impedance of 50 kΩ at 1 kHz, charge injection capacity of 10 mC/cm^2, and a large potential window of 3V.[108] Previously, charge injection capacities of 10-100 μC/cm^2 for NCD[112] and 250-300 μC/cm^2 for nitrogen-doped UNCD[113] were reported. This study demonstrated a significant advancement of the recording and stimulating capabilities of BCND.

The continued advancement of NCD-based electrodes shows a great promise for highly sensitive, stable and biocompatible bioelectrical interfaces capable of recording and stimulating electrical activity of excitable cells.

Graphene

Graphene is a one-atom thick 2D honeycomb arrangement of sp^2-hybridized carbon lattice.[116, 117] Graphene and its derivatives have emerged as promising building blocks for bioelectronics due to their exceptional physical and chemical properties including high electrical

conductivities, outstanding mechanical strength and flexibility, high transparency, high surface area, high chemical stability and tunability.[117-122] In the following sections, we will be discussing three different forms of graphene that are been explored for bioelectronics, i.e. 2D planar graphene, porous graphene, and out-of-plane/vertical graphene.

2D planar graphene

Since the discovery of planar monolayer graphene,[116] there has been an immense interest in its use for various applications including bio-interfaces due to its outstanding electrical conductivity (charge carrier mobility up to 200,000 $cm^2 V^{-1} s^{-1}$), mechanical flexibility, and high transparency of up to 97.7%.[117, 123] In this section, we will discuss the common methods for graphene synthesis, the effect of graphene on cell behavior, and graphene-based bioelectronics to investigate electrophysiology of excitable cells and tissues.

Graphene synthesis

Planar graphene can be obtained using several methods, such as: (i) mechanical exfoliation that involves the use of scotch tape to isolate monolayer graphene sheet from the highly ordered pyrolytic graphite (HOPG);[116] (ii) chemical exfoliation, which involves formation of graphene oxide (GO) suspension from graphite using Brodie, Staudenmaier, or Hummers method, followed by formation of thin films, and reduction of the GO to graphene using thermal, UV or chemical methods;[120, 124, 125] (iii) epitaxial growth on silicon carbide (SiC), which involves thermal decomposition of SiC at 1200-1700 ^oC under high vacuum;[126] and (iv) CVD, a surface-catalyzed process that involves decomposition of C precursor gases such as CH_4, on transition metals such as Ni, Co, and Cu-based substrates at elevated temperatures of ca. 1000 $^\circ C$ either under ambient pressure (APCVD) or low pressure conditions (LPCVD).[119, 127, 128]

Graphene film produced by mechanical exfoliation is the cheapest way to produce high quality graphene, however, graphene production is labor intensive and not scalable, and the flake size is restricted to <1000 μm^2.[127] Chemical methods provide low-cost synthesis and fabrication of large-scale films, however, these assembled graphene films show relatively inferior electrical conductivity owing to the poor interlayer junction contact resistance and the structural defects formed during the exfoliation and reduction processes.[119] Thermal decomposition of SiC yields relatively large graphene sheets on insulating substrates, however, it is not transferrable to other substrates, thus impeding the usage of graphene for flexible and transparent devices. CVD process, on the other hand, enables controlled synthesis of high quality defect-free monolayer graphene. Furthermore, CVD synthesized graphene is transferrable to any substrate of interest using wet transfer and dry transfer techniques.[129-131] Unlike the mechanical exfoliation method, chemical exfoliation and CVD processes require cleaning procedures prior to interfacing graphene with biological samples. The cleaning process are mainly done to remove impurities, such as metal catalyst and the chemicals used during synthesis.

Graphene Biocompatibility

Despite the outstanding properties, the prospective use of graphene in a biological context requires interaction of graphene with cells and tissues to be minimally toxic. The potential toxicity of graphene in biological systems has generated growing debate in recent years due to mixed findings.[132, 133] In the case of cytotoxicity, hemolytic activity on red blood cells and generation of oxidative species in adherent skin fibroblasts due to graphene sheets was reported.[134] Cytotoxic effect of graphene on phaeochromocytoma (PC-12) cells was also demonstrated.[135] High toxicity of pristine graphene was also reported on monkey renal cells, macrophages and red blood cells due to high oxidative stress, which was averted by surface

functionalization of graphene by carboxyl groups.[136, 137] Modification and functionalization of graphene and its derivatives has been done to inhibit acute and chronic toxicity.[133, 138] On the contrary, there have been reports that suggest that graphene is biocompatible with fibroblast cells.[139] Graphene was also found to promote growth, proliferation, and adhesion of mammalian colorectal adenocarcinoma HT-29 cells, human osteoblasts, and mesenchymal stromal cells.[140, 141] Graphene has also been shown to promote differentiation and growth of neurons.[142-144]

One of the major reasons behind mixed findings is the material preparation, i.e., the synthesis and the transfer processes of graphene. Graphene preparation can influence its physicochemical properties, such as size distribution (and lateral dimension), surface chemistry (i.e. surface functional groups and surface charge) and purity. These properties can affect the graphene-cell interactions.[145] Other factors that can explain the contradictory findings are: first, the type of assay used, e.g. the most commonly used viability assay, the MTT assay, has been shown to indicate a false biocompatibility as graphene reacted with MTT to form purple formazon, a result that would indicate viable cells even though there were no cells in this control sample;[134] and second, most of the studies focus on the viability assays, however, these assays are not sufficient indicators of cell health, i.e. whether the cell is under stress.

Recently, a detailed investigation of graphene's biocompatibility was reported by assessing the effect of CVD grown monolayer graphene on cell stress using three highly sensitive intracellular indicators: mitochondrial membrane potential (MMP), mitochondrial morphology, and autophagy levels.[123] MMP plays an important role in maintaining the proton gradient across the mitochondrial membrane which is lost when the cell is under stress.[146] In healthy cells, mitochondria have branched tubular structures which under stress lose the connectivity and form short, round puncta-like structures.[147] Autophagy, a tightly regulated

cellular pathway involving the intracellular degradation of cytoplasmic organelles or cytosolic components, provides another reliable and sensitive indicator of cell stress.[148] During autophagy, a cytosolic form of microtubule-associated protein 1 light chain 3 (LC3) called LC3-I, binds to phosphatidylethanolamine to form LC3-phosphatidylethanolamine conjugate called LC3-II, which translocates to double-membraned vesicles called autophagosomes.[148] Stress conditions, such as nutrient deprivation, induce high levels of autophagy in the cell that can be quantified by the significant increase in autophagosome vesicles.[149]

In that study,[123] the effect of LPCVD synthesized monolayer graphene substrates on the viability and stress of monkey renal fibroblast (Cos7) cells and primary E18 rat hippocampal neurons was investigated. Viability assays, performed using calcein acetoxymethyl and ethidium homodimer dyes, showed that graphene substrates promoted healthy proliferation and confluency of the Cos7 cells and healthy maturation of neurons. To determine the effect of graphene on MMP and mitochondrial morphology, tetramethylrhodamine ethyl ester (TMRE), a quantitative fluorescence marker for the activity of mitochondria, was used. No significant difference in the MMP and similar tubular morphology of mitochondria in the cells cultured on both glass and graphene substrates confirmed that graphene does not induce cell stress (Figure 5A-C). To determine the autophagy levels, the cells were transfected with red fluorescent protein fused LC3 (RFP-LC3) plasmid DNA to quantify autophagosomes.[150] No significant difference in autophagosome puncta in the cells cultured on graphene and glass control substrates, and significantly low number of autophagosomes in the cells cultured on graphene substrates compared to cells under nutrient starvation, validated that graphene does not induce cell stress (Figure 5D-F). This study demonstrated an in-depth analysis of graphene's biocompatibility, and thus highlighted the potential of graphene to be used for long-term stable bioelectronics.

Graphene Bioelectronics

The high transparency of planar monolayer graphene can enable simultaneous optical studies for both electrophysiology applications such as Ca^{2+} imaging and optogenetic manipulation of the cells,[151] and non-electrophysiology applications such as optical coherence tomography (OCT) imaging,[152] monitoring biochemical activity of the cells using fluorescently labeled dyes and proteins,[153-155] and further investigation of the tissue health[123] at the electrode-cell interface over time. Other nanocarbons such as CNTs[50] and NCDs[87] have been also explored for transparent electrodes, however, their transparency is limited by the concentration of CNT used and the doping concentration, respectively. Studies have shown usage of indium tin oxide (ITO)[156], bilayer nanomesh[157]-based electrodes as transparent platforms, however, they are either limited by the brittle nature of the electrode material or by the limited transparency over a wide spectral range. High mechanical flexibility, high transparency of ca. 97.7 % over wide spectral range, and high biocompatibility of graphene makes it a better candidate for transparent devices.

FETs fabricated with mechanically exfoliated graphene demonstrated, for the first time, recorded extracellular field potentials of spontaneously beating embryonic chick cardiomyocytes (Figure 6A).[158] Graphene FETs have an advantage due to their ambipolar behavior that enables both n- and p-type recording with the same device. This characteristic was validated by signal shape flip of recorded extracellular potentials across the Dirac point. In addition, graphene FETs showed better performance compared to other planar devices by yielding extracellular signals with SNR >4.[158] The measured signal was demonstrated to be dependent on the size of the graphene flake. A large graphene FET with active channel of 20.8 μm × 9.8 μm recorded signals with peak-to-peak width of 1.31 ± 0.04 msec. Whereas, signals recorded from a much smaller graphene FET with active channel dimensions of 2.4 μm × 3.4 μm yielded peak-to-peak width of

0.73 ± 0.04 msec, two times smaller than that obtained from the larger device. These results indicated that the signals recorded with the larger graphene device represent an average of the extracellular potential from sufficiently distinct sources of the beating cell. Following this pioneering work, electrical recording of HL-1 cells were also demonstrated using graphene FETs fabricated using CVD grown graphene.[159] A variety of peak shapes were reported, which were attributed to variations in the cell-graphene device junctions. The multiplexed data also yielded signal propagation speeds of 12-28 μm/msec. Interestingly, FETs with suspended graphene as channel were shown to represent the optimal configuration for cardiac extracellular electrophysiology in terms of transducer sensitivity, ca. five times higher than substrate-supported devices cell-device coupling.[160]

Planar graphene-based MEAs have been explored for electrophysiological investigation of excitable cells.[121, 152, 161, 162] The high flexibility of graphene has enabled fabrication of electrodes on flexible substrates,[152, 161] and high transparency has enabled simultaneous optical and electrical recordings from excitable cells and tissues.[121, 161] Recently, MEA fabricated using LPCVD synthesized monolayer graphene was demonstrated for Ca^{2+} and electrical recordings of human embryonic stem cells-derived cardiomyocytes (hESC-CMs) (Figure 6B,C).[121] Tunable properties of graphene was shown by nitric acid treatment, and stable electrical recordings of field potentials were demonstrated with high SNR of >14, comparable to that of standard Au electrodes. In addition, the high temporal resolution provided information about the Na^{+} current (upstroke), K^{+} current (repolarization) and Ca^{2+} current (plateau phase) across the cell membrane. The transparency of graphene electrodes also enabled Ca^{2+} imaging at the electrode-cell interface unlike metal-based electrodes. The integration of temporal resolution and spatial advantages of electrical and optical recordings at the electrode-cell interface was demonstrated.

Furthermore, the application of β-adrenergic agonist, isoproterenol, led to an increase in the beat frequency and a decrease in the duration of the field potentials recorded by graphene electrodes.[121] This suggested that graphene MEA platform can be used to detect changes in electrophysiology which is crucial for both diagnostic and therapeutic platforms.

In conclusion, the studies reported above show that monolayer graphene enables fabrication of transparent, flexible and biocompatible bioelectronics. It also enables integration of advantages of multiple techniques i.e. electrical and optical, in one system thus making it a powerful tool to understand and develop therapeutics for diseases such as Alzheimer, Parkinson's disease and arrhythmias.

Porous graphene

High transparency of planar graphene makes it an attractive material for bioelectronics, however, the low surface area due to its 2D planar structure limits its use as ultra-microelectrodes for sub-cell recordings and electrical stimulation. High surface area is crucial to enhance electrochemical activity, reduce the electrode impedance, and enhance the charge storage and injection capacities of stimulation electrodes. Recently, porous graphene materials have gained interest due to their large accessible surface area. In this section, we will briefly discuss the different synthesis methods for porous graphene, and the effect of porous graphene-based substrates on cell proliferation and differentiation. We will then summarize the studies that demonstrated the use of porous graphene for electrical recording and stimulation of the excitable cells.

Porous graphene synthesis

In the past decade, 3D porous graphene structures have been synthesized by various methods. Self-assembly of GO nanosheets has been widely applied to prepare 3D graphene structure, e.g. formation of 3D graphene hydrogel using hydrothermal treatment of GO suspension[163] and chemical reduction of GO in water.[164] 3D graphene has also been synthesized by templated methods, such as (i) template-directed assembly, e.g. use of polystyrene (PS) colloidal spheres to form graphene/PS composite followed by dissolution of PS template in toluene to form 3D graphene foam with uniform pore structures;[165] and (ii) template-directed CVD, e.g. graphene synthesis on a Ni foam template, followed by etching of the scaffold.[164] 3D porous graphene films have also been achieved from polymer substrates such as polyimide films using laser scribing methods.[166] The laser irradiation results in lattice vibrations leading to extremely high localized temperatures (>2,500 °C). The high temperature breaks the C-O, C=O and N-C bonds and leads to rearrangement of aromatic compounds to form graphitic structures.[166]

Porous graphene-cell interfaces

High conductivity, porous topography and high surface area makes porous graphene a promising material for cell interfaces. The use of porous graphene synthesized using Ni foam assisted CVD process was reported as a scaffold for neural stem cells (NSC) growth.[167] The high biocompatibility of porous graphene as well as enhancement in the NSC differentiation towards astrocytes and neurons compared to planar graphene was demonstrated. In addition, porous graphene provided an efficient conductive platform to mediate electrical stimulation for differentiated NSC.[167] Porous graphene was also demonstrated to support the attachment and viability of human mesenchymal stem cells, and induce spontaneous osteogenic

differentiation.[168] These studies show the potential of porous graphene in the field of tissue engineering as well as bioelectronics. However, it is essential to perform further investigations of the effect of porous graphene, synthesized using various methods, on the viability and health of cells and tissues since different synthesis techniques in the case of monolayer graphene and CNTs have shown to have varying effects on cells.

Porous graphene bioelectronics

The high accessible surface area of porous graphene has made it an attractive material for biosensing applications such as detection of neurotransmitters,[169-173] glucose,[174] nucleobases,[175] and proteins.[176] Recently, the use of porous graphene has been explored as a platform for electrophysiological investigations. The use of CVD synthesized porous graphene as the extracellular matrix for the growth as well as monitoring of extracellular potential of the HL-1 cells was demonstrated.[177] More recently, a flexible cortical MEA using porous graphene, which was directly synthesized on polyimide substrate using laser pyrolysis, was reported (Figure 7A).[178] The high density porous graphene-based MEAs fabricated on polyimide substrate exhibited high mechanical flexibility, drastically lower impedance, and high charge injection capacity. The *in vivo* electrical recordings were demonstrated by placing a 16-electrode array on an exposed cortical surface (Figure 7B I). Electrical recordings from one of the electrodes showed spontaneous up and down states of barrel cortex activity, implying active and inactive states of neuronal networks (Figure 7B II). The average power spectral density exhibited three prominent oscillations with center frequencies of 0.8 Hz, 40 Hz, and 90 Hz that correspond to delta, low gamma, and high gamma rhythms, physiological oscillations generated by the brain (Figure 7B III). The electrodes also enabled recording of somatosensory-evoked potentials from the pial surface of barrel cortex. The porous graphene arrays were also explored for cortical

micro-stimulation. The electrode array was placed over motor cortex and the stimulus trains were applied to a rat to evoke transient ankle and knee flexion in the contralateral leg (Figure 7C I). Higher current stimulus led to stronger movement without inducing any tissue damage (Figure 7C II). The study demonstrated the potential of using graphene-based electrodes for micro-stimulation that could improve the efficiency of clinical treatments, such as deep brain stimulation for Parkinson's and responsive neuro-stimulation for epilepsy.

Out-of-plane growth of graphene flakes

An alternative approach to achieve the 3D surface topology is to perform out-of-plane or vertical growth of graphene flakes, thus exposing both sides of the graphene sheets. In this section, we will discuss the various synthesis methods to obtain vertical graphene and fuzzy graphene, and their current and potential applications for cell-nanomaterial interfaces and bioelectronics.

Out-of-plane graphene synthesis

Out-of-plane graphene flakes have been synthesized using various methods, such as: (i) thermal decomposition of SiC to synthesize large-area vertically aligned graphene sheets (VAGS)[179, 180] and (ii) PECVD for catalyst-free vertical growth of carbon nanowalls (CNWs).[181-183] The VAGS and CNWs are generally composed of few to dozens of graphene layers tethered to a 2D surface. Due to the out-of-plane morphology, the specific surface area of these materials is significantly higher as compared to planar graphene. However, in both cases the out-of-plane graphene flakes are still tethered to the surface.

Recently, a highly-controlled out-of-plane synthesis of single- to few-layer 3D fuzzy graphene (3DFG) on a 3D Si nanowire (SiNW) mesh template was demonstrated to further

enhance the 3D morphology that leverages graphene's outstanding surface-to-volume ratio.[122] The synthesis of NW-templated 3DFG (NT-3DFG) hybrid nanomaterial involved three-step process: first, synthesis of SiNWs by the Au nanoparticle catalyzed vapor-liquid-solid (VLS) process; second, formation of an interconnected mesh by collapsing and annealing the SiNWs; and third, synthesis of 3DFG on the SiNWs mesh through inductively coupled PECVD process. Various synthesis conditions such as CH_4 partial pressure and PECVD process time were explored to demonstrate the tunability of the 3DFG flake size and density. The SEM and TEM characterization confirmed the out-of-plane growth of 3DFG flakes from the surface of SiNW (Figure 8A, B). Selected area electron diffraction (SAED) data indicated the polycrystalline nature of 3DFG. The presence of characteristic peaks in the Raman spectra, i.e., D, G, and 2D peaks, confirmed the presence of graphene (Figure 8C). A detailed Raman analysis was performed to investigate the effect of flake size and density on the intensity ratios of the peaks.[122] Dual-laser Raman characterization confirmed that the sharp D peak in the Raman spectra was due to presence of graphene edges.[122] The electrical and electrochemical characterizations of NT-3DFG (Figure 8D) showed exceptional electrical conductivity of up to 2355 ± 785 S m^{-1} (59 ± 12 Ω $□^{-1}$), and high electrochemical surface area of up to 1017 ± 127 m^2 g^{-1}, significantly higher than other reported forms of CNT and graphene-based materials.[122]

Out-of-plane graphene-cell interfaces

Even though graphene has been shown to be biocompatible with both nonneuronal and neuronal cells, it is crucial to investigate the effects of out-of-plane graphene on cell behavior owing to the differences in physical properties of the nanomaterials. The presence of sharp edges in the vertical graphene-based substrate was demonstrated to damage the cell membrane of the bacteria upon direct contact thus leading to bacterial inactivation.[184] High biocompatibility of

CNWs and high cell proliferation of osteoblasts was demonstrated on CNW-based scaffold.[185] In addition, the nanotopography of CNW led to more elongated cell morphology compared to cells cultured on tissue culture polystyrene.[186] The effect of CNWs with and without functionalization has also been investigated on cell proliferation, morphology and cytokine secretion of macrophages.[185] High biocompatibility of CNWs was demonstrated. An enhancement in the cell adhesion and acute inflammatory response was observed post-modification of CNW with oxygen plasma as demonstrated by the increased release of cytokines.[185]

These studies demonstrated high biocompatibility of vertically grown graphene and increased proliferation and adhesion of cells on these substrates. Investigating the cell-graphene interfaces further by using techniques such as focused ion beam scanning electron microscope (FIB-SEM) can provide better insights about the interaction. In addition, it will be intriguing to investigate the effect of nanotopography combined with electrically conductive cues of these nanomaterials on the maturation and functional properties of excitable cells.

Out-of-plane graphene-bioelectronics

The high surface area of vertically grown graphene sheets make them a potential candidate for their use in bioelectronics. The vertical graphene FETs have been developed as biosensors.[187] Fabrication of FET sensor by direct growth of vertical graphene (VG) sheets on gold electrodes using the PECVD method was demonstrated. In addition to high surface area, the vertical structure of VG facilitated the deposition of the Au NP-antibody conjugates on the sensor. The VG-based biosensor showed a high sensitivity with detection limit as low as 13 pM, and high selectivity towards specific proteins.[187] Recordings of neuronal activity from primary mice hippocampal neurons cultured on carbon nanosheets (CNS) was demonstrated.[188] PECVD-synthesized CNS were patterned on TiN electrodes, and the performance was compared with

bare TiN electrodes. The modification with CNS led to an increase in the double layer capacitance by a factor of 10, and the charge storage capacity by a factor of 5. In addition, there was a two-fold increase in SNR of action potentials measurements from hippocampal neurons measured using CNS coated TiN electrodes compared to standard TiN electrodes with the same dimensions.[188]

The studies demonstrated how the morphology of graphene can affect the performance both for sensing and recording applications. Nonetheless, the out-of-plane graphene has not been explored much for electrophysiological applications, especially as stimulation electrodes. The high charge capacities due to enhanced surface area makes this material a good candidate to be used for electrical stimulation of excitable cells. In addition, it would be intriguing to investigate how changing the flake size and density of these vertically grown graphene, shrinking the geometric size of the electrode, and surface modifications such as nitric acid treatment, will affect its recording and stimulation capabilities.

CONCLUSIONS AND OUTLOOK

In this review article, we have summarized the properties, synthesis methods, cell-nanomaterial interfaces, and applications in bioelectronics of different forms of nanocarbons. Each kind of nanocarbon has certain advantages and disadvantages associated with it. Compared to planar graphene and NCDs, CNTs have a higher surface area due to their cylindrical structures. However, one of the major challenges in scaled-up CNTs synthesis methods is the presence of mixed population in terms of electrical and mechanical properties, whereas, NCD and graphene synthesis techniques result in more uniform samples. NCDs show excellent chemical stability, water window potential, and higher surface area than planar graphene, but require doping to enhance the conductivity, which decreases transparency. Graphene and CNTs,

however, do not require doping for high electrical conductivity. Doping can be used to enhance desired electrical or electrochemical properties. Planar graphene has an advantage of being transparent, however, it is limited by the surface area due to its planar nature. Whereas, the bulk structure of 3D graphene leads to poor transparency when compared to planar graphene, however, it has an advantage of having significantly higher surface-to-volume ratio, which is essential for both low impedance and high charge capacities. The carbon nanomaterials detailed in this paper show bioelectronic properties on par with metal electrodes such as gold and platinum and nanomaterial-based FETs such as SiNWs [Table 1]. Nanocarbons offer unique advantages including high surface area, high conductivity, transparency, large electrochemical water window, and high potential for multifunctional modalities. CNTs, porous graphene, 3D graphene, and NCDs can be used for both stimulation and recording, while planar graphene can be used for simultaneous optical and electrical modalities. These materials exhibit high sensitivity in biosensing applications, suggesting the potential for combined sensing and electrophysiology. Last, carbon-based materials can be used to fabricate both MEAs (passive) and FETs (active) sensors [Table 1].

Advances in technology and methodology are crucial aspects of cutting-edge science. The ability to investigate the electrophysiology of excitable cells and tissues has advanced the fields of cardiology and neuroscience in understanding of the circuitry and functioning of both healthy and diseased cellular networks. However, there are still a few major bioelectrical challenges that will need to be addressed in the next few years: (i) to provide seamless integration of the electrodes with the cells and tissues to record electrical activity at high SNR and enable long-term stable interfaces without interfering with the normal functionality of the tissue; and (ii) to fabricate electrodes with single cell and sub-cellular dimensions to enable high

precision, avoid averaging of signals, and enable high density of electrodes for multiplex recordings from dense cellular networks. Recently, the use of 3D nanocarbons has enabled fabrication of low impedance electrodes due to the net high surface area. This is crucial to enable shrinking down the geometric size of the electrodes to the dimensions comparable to single cell. The hybrid-nanomaterials such as the NT-3DFG can further push the limits down to few microns or even lower due to their extraordinary electrical conductivity and surface area. In addition, the tunable porosity and flake size and density can further allow tailoring of the nanotopography which is crucial for cell-substrate adhesion, thus further improving the electrical coupling at the electrode-cell interface.

A promising route in the field of bioelectronics is the development of smart hybrid-materials with multifunctional modalities, such as electrical recording, stimulation, biomolecule sensing, and delivery of molecules such as therapeutic drugs. Having all these capabilities in one system will make a powerful tool to enable greater insights into complex biological systems functionality, cardiac and neurological disease progression, and potential new therapeutic directions.

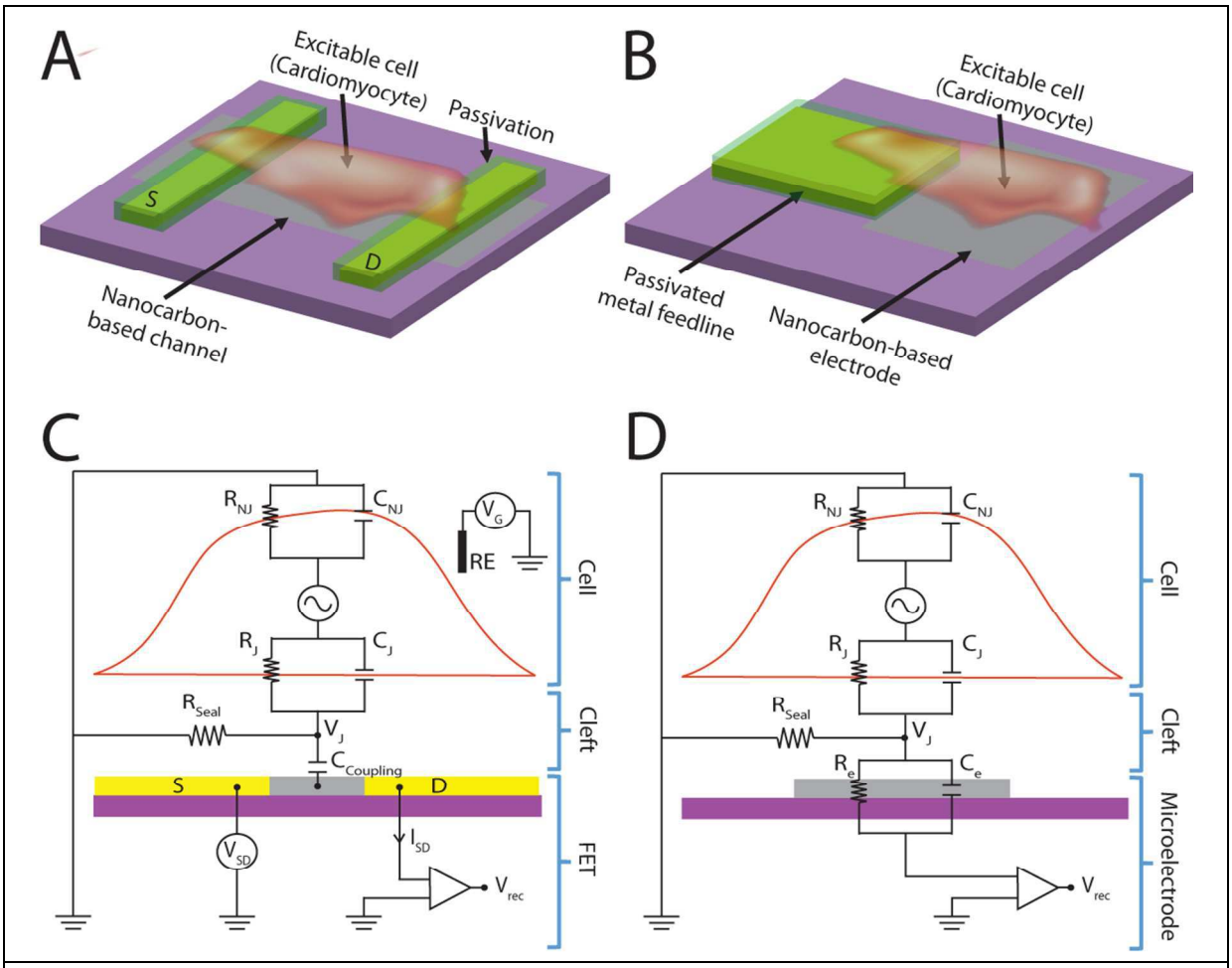

Figure 1. Schematic of the recording platforms. Schematic illustrating the interface of excitable cells with **(A)** FET and **(B)** MEA. Electrical equivalent circuit of the **(C)** cell-FET and **(D)** cell-microelectrode interfaces. S and D represent source and drain leads, respectively. R_J, R_{NJ}, R_{Seal}, and Re represent junctional, non-junctional, seal and electrode resistances, respectively. C_J, C_{NJ}, $C_{Coupling}$, and C_e represent junctional, non-junctional, coupling, and electrode capacitances, respectively. V_J, V_{SD}, V_G, V_{rec} and I_{SD} represent junctional voltage across the cleft, source-drain voltage, gate voltage, recorded voltage, and source-drain current, respectively. RE represents reference electrode.

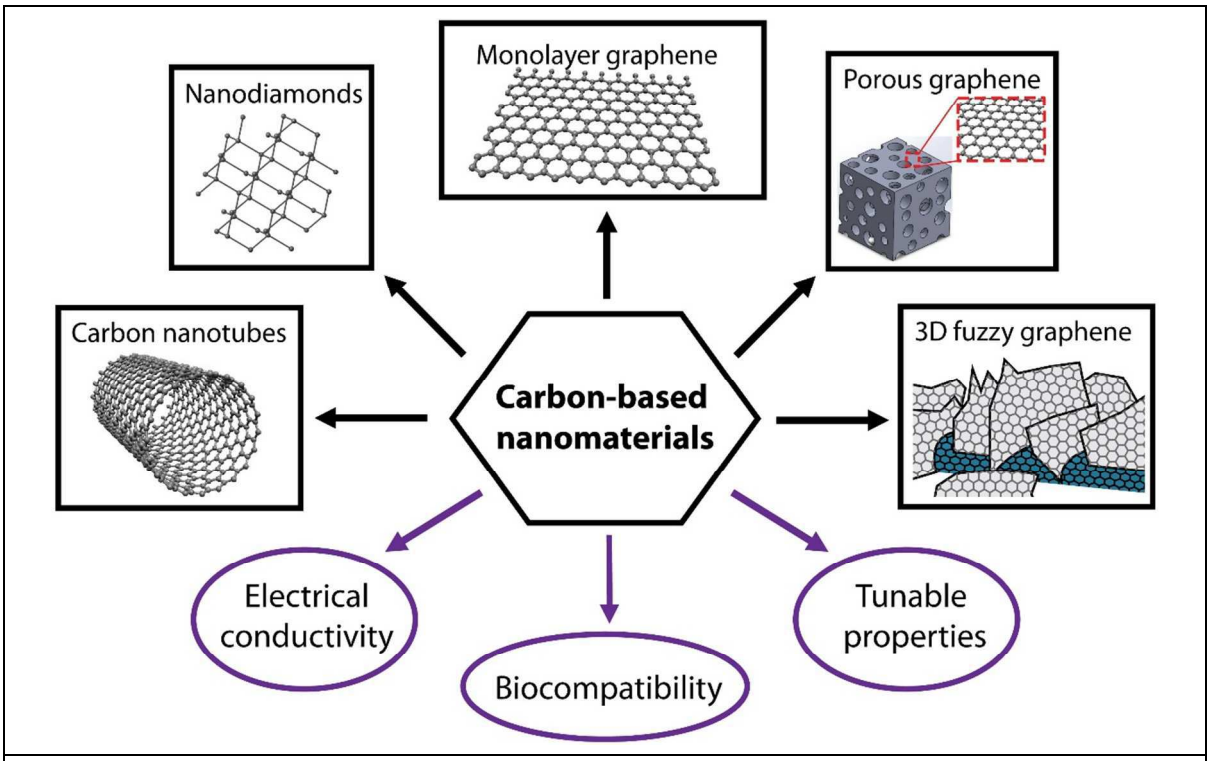

Figure 2. Various nanocarbons and their key advantages in bioelectrical interfaces.

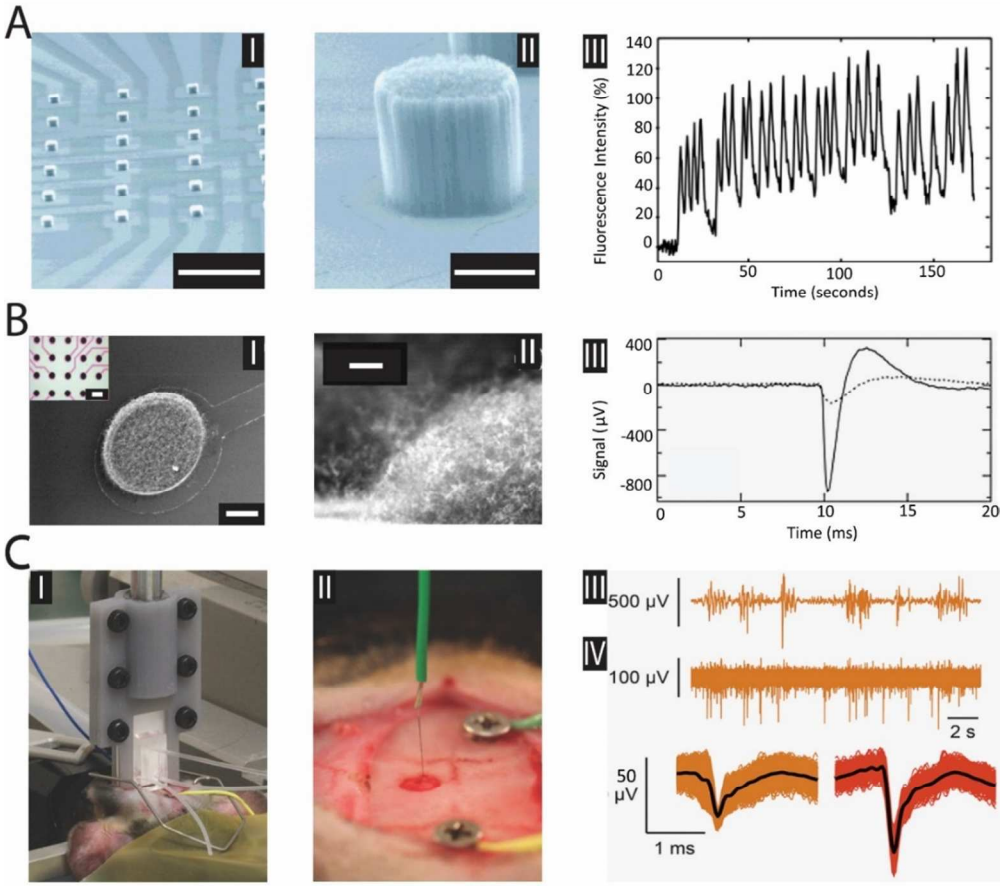

Figure 3. Electrical stimulation and recording using carbon nanotube (CNT)-based electrodes. (A) CNT microelectrode array (MEA) for neural stimulation. (I) Image of a MEA on patterned doped polysilicon conductive layer with CNT self-assembled pillars. Scale bar: 500 μm. (II) Vertically aligned CNTs form a 50 μm protruding electrode. Scale bar: 25 μm. (III) Action potentials detected optically by tracking fluorescence intensity upon intracellular calcium concentration changes in embryonic rat hippocampal neurons with repeated electrical stimulation using CNT MEA. **(B)** CNT MEA for extracellular neural recording. (I) High resolution SEM (HR-SEM) image of a representative 80 μm CNT electrode fabricated on conductive titanium nitride pad. Inset: Optical microscopy image of the array. Scale bars: 20 μm; Inset: 150 μm. (II) Side view HR-SEM image of an individual CNT electrode indicates 3D topology. Scale bar: 10 μm. (III) Spontaneous extracellular signal recorded using CNT electrode from rat cortical neurons cultured on the MEA. **(C)** Fluidic microactuation of flexible carbon nanotube fiber (CNTf) electrode for neural recording. (I) Microfluidic device delivers flexible CNTf microelectrode into the mouse brain at precise location and depth. (II) Photograph of CNTf 22 μm electrode in the rat brain. Two skull screws were implanted for electrical reference and to monitor cortical EEG activity. (III) EEG signal from screw located on the right frontal cortex. (IV) Spontaneous unit activity recorded with CNTf at 3.75 mm depth; below are clustered spikes from the recording trace. Reproduced with permission using figures from (A) Wang, K., *et al*., *Nano Lett.,* 2006,[43] (B) Gabay, T., *et al.*, *Nanotechnology,* 2007,[44] and (C) Vitale, F., *et al*., *Nano Lett.,* 2017.[59]

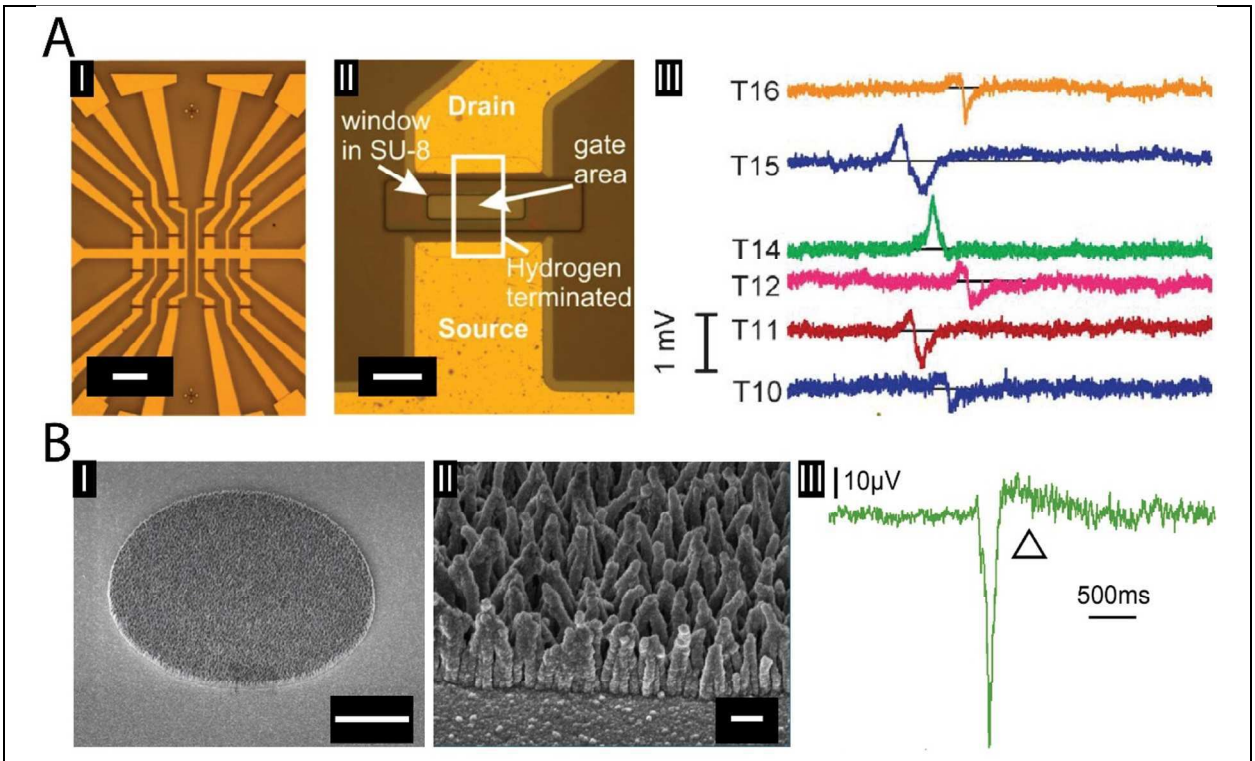

Figure 4. Electrical recording using nanodiamond-based electrodes. (A) Solution-gated field-effect transistors (SGFET) made with hydrogen-terminated single crystal diamond for electrical recording of HL-1 and HEK293 cells. (I) Image of 4 x 4 SGFET array. Scale bar: 200 µm. (II) Expanded view of SGFET, highlighting the channel, and source and drain electrodes. Scale bar: 20 µm. (III) Field potential recordings using transistors interfaced with HL-1 cells. T10-T16 correspond to specific transistors. **(B)** Three-dimensional (3D) nanostructured boron-doped diamond (BDD) microelectrode array (MEA) for neural recording. (I) Low and (II) high magnification images of 3D nanostructured BDD electrode fabricated by complete encapsulation of vertically aligned carbon nanotubes (VACNTs) in BDD. Scale bars: 20 µm and 1 µm. (III) Local field potentials recorded using the BDD electrode. Reproduced with permission using figures from (A) Dankerl, M., *et al., Adv. Funct. Mater.,* 2009,[109] and (B) Piret, G., *et al., Biomaterials,* 2015.[108]

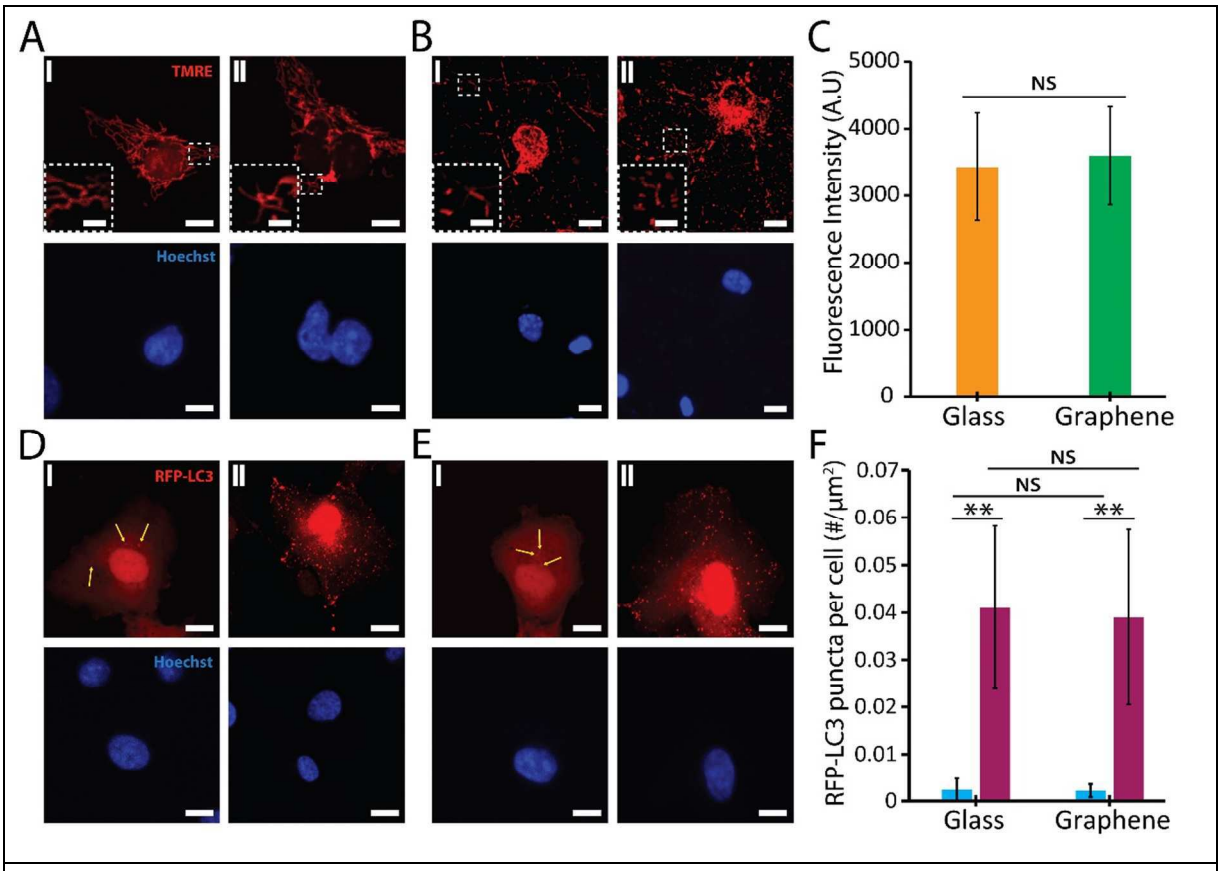

Figure 5. Biocompatibility of monolayer graphene. (A-C) TMRE assay performed on cells cultured on (I) glass and (II) graphene substrates. High magnification single cell confocal images of **(A)** Cos7 cells and **(B)** primary hippocampal neurons labelled with TMRE for mitochondria (red) and Hoechst for nuclei (blue). Insets: Expanded view of the marked white dashed area. Scale bars: 10 μm; Insets: 2.5 μm. **(C)** Relative fluorescence readout of the TMRE-labeled cells cultured on glass (orange) and graphene (green) substrates. NS denotes no statistically significant difference. Results are presented as mean ± SD (n=3, 50 cells). **(D-F)** Detection of autophagy levels in Cos7 cells cultured in (I) presence of serum (i.e. normal) and (II) absence of serum (i.e. starvation) in the medium. High magnification single cell confocal images of the cells cultured on **(D)** glass and **(E)** graphene substrates labelled with RFP-LC3 for autophagosomes (red) and Hoechst for nuclei (blue). Yellow arrows point to autophagosome puncta. Scale bars: 10 μm. **(F)** Relative RFP-LC3 puncta per cell normalized by the cell area for the cells cultured on glass and graphene substrates, under normal (cyan) and starvation (magenta) conditions. (**) denotes statistically significant difference with $p<0.005$. NS denotes no statistically significant difference. Results are presented as mean ± SD (n=4, 50 cells). Reproduced with permission using figures from (A-F) Rastogi, S.K., *et al*., *Nano Lett.,* 2017.[123]

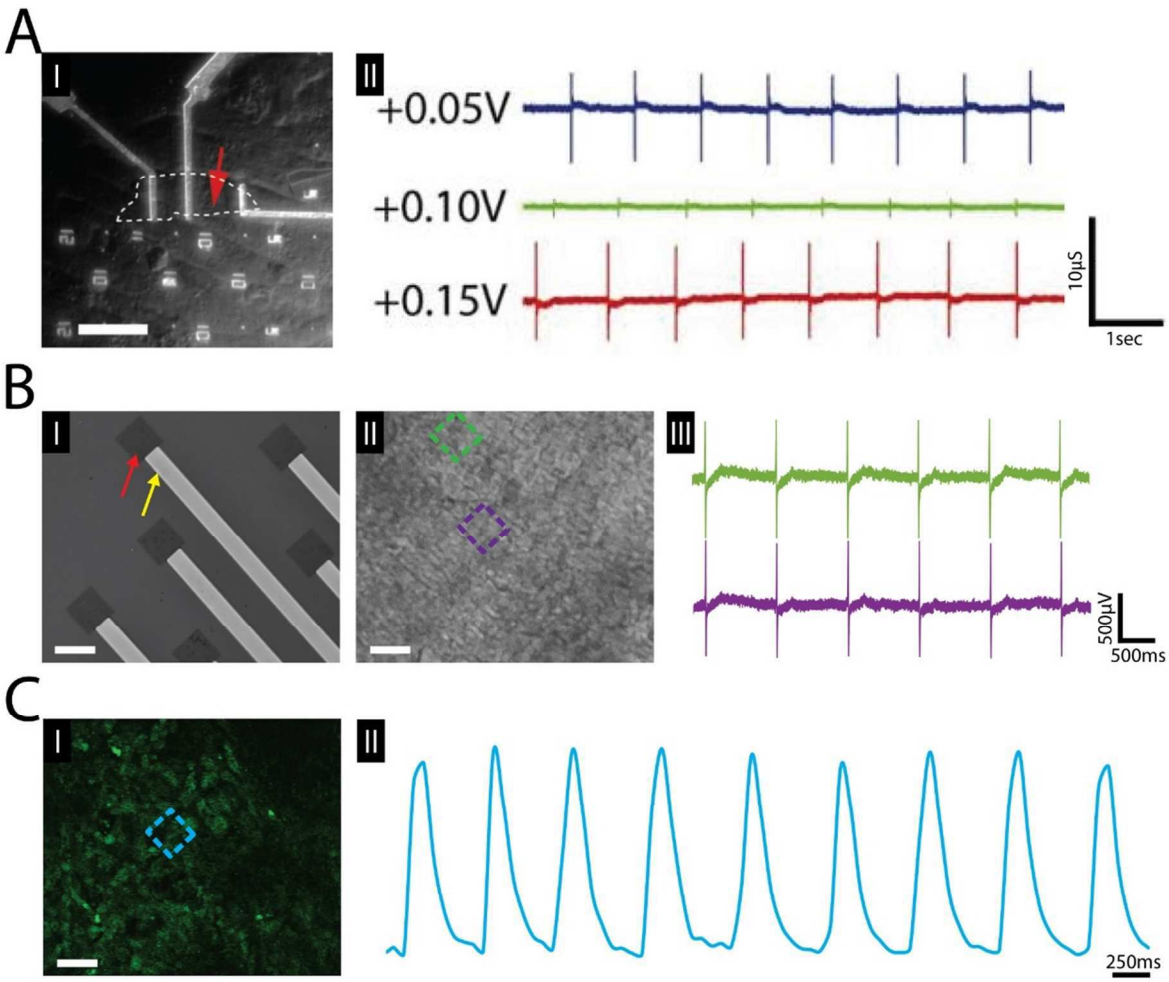

Figure 6. Electrical recording using monolayer graphene. (A) Field potential recording of cardiomyocytes using field effect transistors (FETs) fabricated with mechanically exfoliated graphene. (I) DIC image of cardiomyocytes interfaced with the graphene-FET. White dashed line and red arrow represent graphene flake, graphene-FET device, respectively. Scale bar: 30 μm. (II) Recorded traces at different applied water gate potentials of +0.05 (blue), +0.10 (green) and +0.15 V (red). **(B-C)** Electrical and optical recordings from human embryonic stem cells-derived cardiomyocytes (hESC-CMs) using microelectrode array (MEA) fabricated with graphene synthesized by low pressure chemical vapor deposition (LPCVD). **(B)** Field potential recordings. (I) DIC image of the graphene MEA fabricated on a Si/285 nm SiO_2 substrate. Red and yellow arrows indicate exposed and SU8 passivated graphene electrodes, respectively. Scale bar: 50 μm. (II) DIC image of hESC-CMs cultured on graphene MEA. Scale bar: 50 μm. (III) Representative recorded field potential traces using graphene electrodes marked in (II). **(C)** Calcium fluorescence signal recordings. (I) Confocal image of hESC-CMs loaded with Fluo-4 dye, cultured on graphene electrodes. Scale bar: 50 μm. (II) Fluorescence intensity as function of time at the electrode region marked in (I). Reproduced with permission using figures from (A) Cohen-Karni, T., *et al*., *Nano Lett.* 2010,[158] (B-C) Rastogi, S.K., *et al*., *Cell. Mol. Bioeng.* 2018.[121]

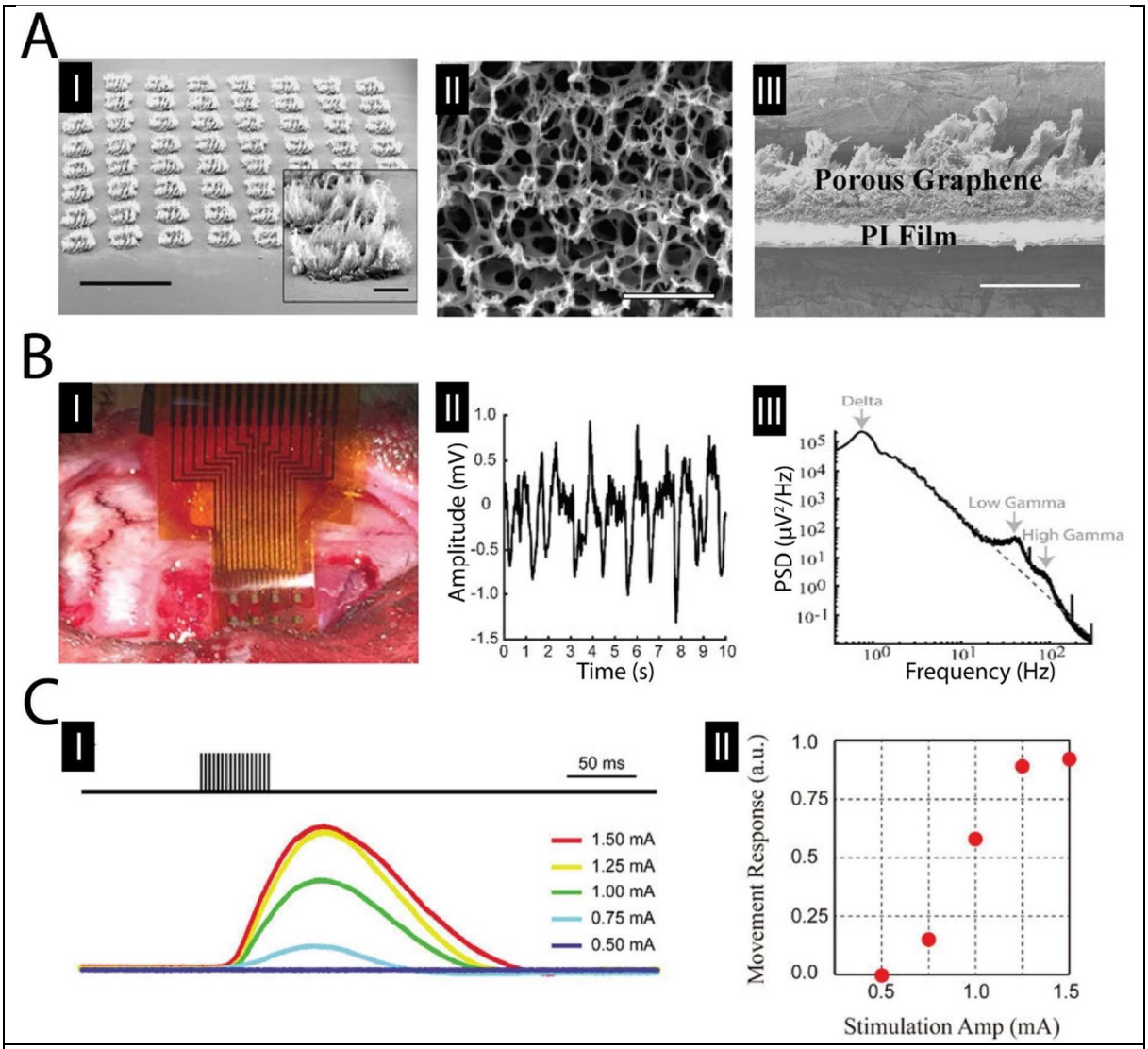

Figure 7. Electrical recording and stimulation using porous graphene. (A) Porous graphene electrode array fabrication. (I) SEM image of a porous graphene electrode array. Inset: SEM image of an individual electrode. Scale bars: 1 mm; Insets: 100 μm. (II) SEM image of the porous morphology of surface. Scale bar: 2 μm. (III) SEM image of the cross-section view of porous graphene. Scale bar: 100 μm. **(B)** *In vivo* electrical recordings. (I) A 16-electrode array placed at the pial surface of the rat's barrel cortex. (II) Representative 10 sec recording trace from an electrode. (III) Average power spectral density of the recorded signal over 5 min. **(C)** *In vivo* stimulation from cortical surface. (I) Stimulus trains with current amplitudes ranging from 0.5 mA to 1.5 mA. (II) Movement response versus stimulation amplitude. Reproduced with permission using figures from (A-C) Lu, Y., *et al*., *Sci. Rep.* 2016.[178]

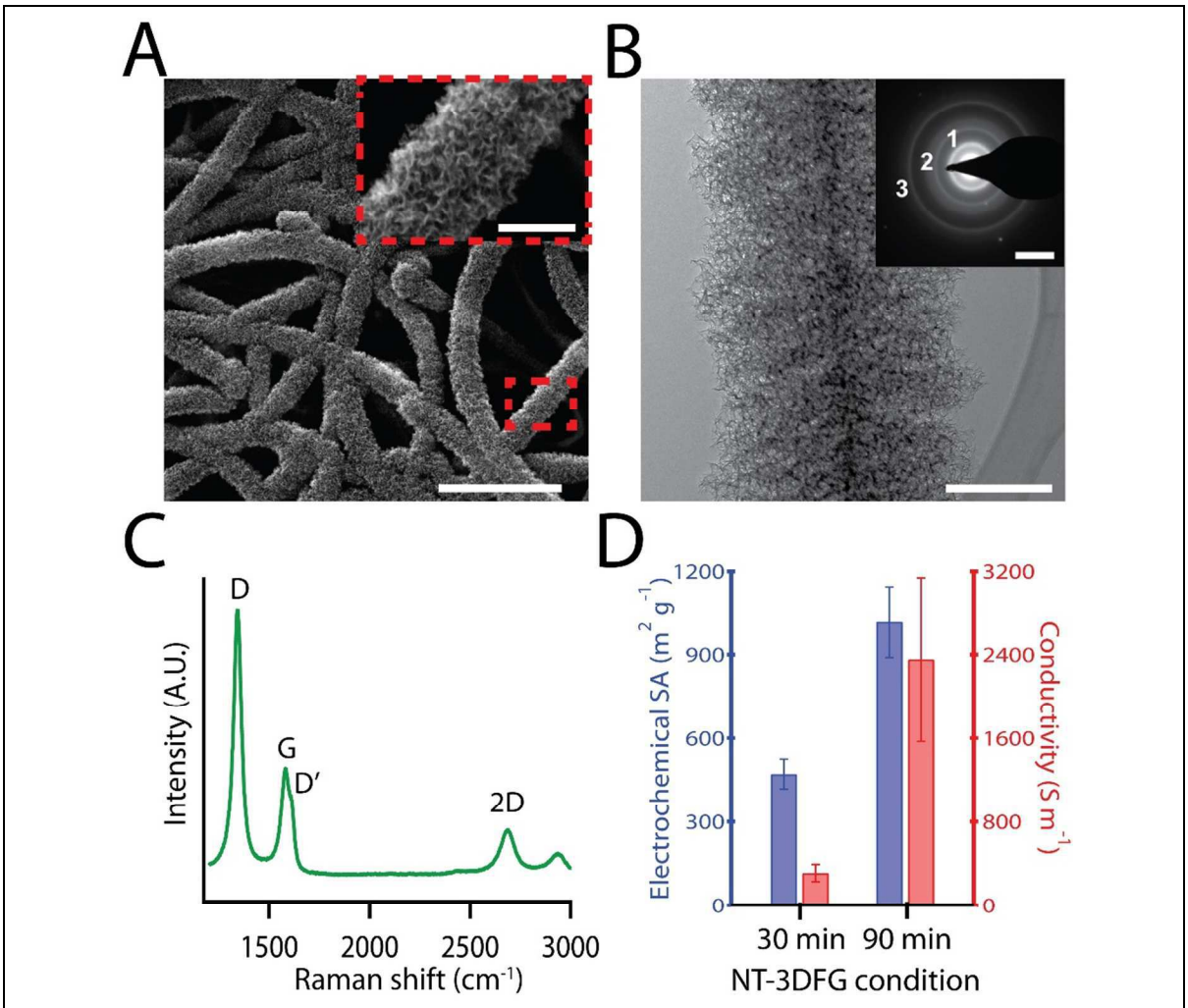

Figure 8. Nanowire templated growth of out-of-plane three-dimensional fuzzy graphene (NT-3DFG). (A) SEM image of NT-3DFG synthesized using plasma enhanced chemical vapor deposition (PECVD) under 25.0 mTorr CH_4 partial pressure for 30 min. Inset: Expanded view of the marked red dashed area. Scale bars: 2 µm; Inset: 250 nm. **(B)** TEM image of NT-3DFG synthesized under 25.0 mTorr CH_4 partial pressure for 30 min. Inset: Representative selected area electron diffraction (SAED) pattern indicating polycrystalline diffraction rings of 3DFG, numbered as 1 ($d_{0002} \approx 0.350$ nm), 2 ($d_{10\bar{1}0} \approx 0.205$ nm) and 3 ($d_{11\bar{2}0} \approx 0.119$ nm). Scale bars: 200 nm; Inset: 5 nm^{-1}. **(C)** Representative Raman spectra of NT-3DFG. **(D)** Electrochemical surface area and conductivity as a function of synthesis time. Reproduced with permission using figures from (A-D) Garg, R., *et al*., *ACS Nano* 2016.[122]

MEAs							
Nanocarbon	**Substrate**	**Area (μm^2)**	**Impedance (kΩ)**	**Amplitude (μV)**	**SNR**	**CIC ($mC\ cm^{-2}$)**	**Reference**
CNT							
MWCNT	PDMS, Polyimide, Parylene C	1962-125664	55	-	20	-	42
Vertically aligned CNTs	Quartz	2500-10000	~2*	-	-	~1	43
MWCNT	Si/SiO_2	5024	10	~1000*	135	-	44
Carbon nanofiber VACNF	Si/SiO_2	~140* (Diameter = 4 μm, Height =10 μm)		50	~2*	-	47
Web-like CNT film	PDMS	10000	~200	~400*	-	-	54
VACNT	Pt/Graphene	~160* (Diameter = 5 μm, Height = 9 μm)	110	~35	~16	-	49
VACNT	Graphene	~160* (Diameter = 5 μm, Height = 9 μm)	390	1600	215	-	50
CNT	Si/SiO_2	707	~2	~196	2030	-	
CNT	Polyimide	7854-125600	-	100-200	~6	-	51
CNTf	-	1450	~11	-	3	~6	58
NCD							
BNCD	Fused silica	314	180	100	-	250	106
BNCD	Tungsten wire	1963	0.4	10-20*	~105	-	110
BNCD	Si	314	-	300-650	-	-	107
3D- BNCD	Si	314	50-100	10-20*	-	10	108
Graphene							
CVD graphene	Polyimide	2500	~2000 (~500 post nitric acid)	~2500*	~40	-	161
CVD graphene (4 layers)	Parylene C	31416	~240	-	-	-	152
CVD graphene	Polyimide	31416	~100	~1000	65	-	162

CVD graphene	glass, Si/SiO_2	2500	~2100 (~1500 post nitric acid)	~800	14	-	121
porous graphene	Polyimide	62500	~5	-	-	~3	178
vertical graphene nanosheet	Si/SiO_2	314 (1963 for cell recording)	400	~200*	~5	-	188
Other materials							
Au	Polyimide	250000	~17	~2500*	~8	-	161
Au	Si/SiO_2	2500	~1200	~800	17	-	121
Au	Si/SiO_2	707	~600	~25	10	-	51
TiN	Si/SiO_2	707	~36	~60	207	-	51
FETs							
Nanocarbon	**Substrate**	**Size (μm^2)**	**Mobility ($cm^2 V^{-1} s^{-1}$)**	**Amplitude (μV)**		**SNR**	**Reference**
NCDs							
H terminated Diamond	-	100-400	50	~1000		-	109
Graphene							
Exfoliated graphene	Si/SiO_2	~200	Holes: 4000 Electrons: 3550	~3600		≥4	158
CVD graphene	Sapphire	200	-	~900		≥10	159
Exfoliated graphene	Suspended	3-17	-	22000		-	160
Si nanowires							
SiNW	Si/SiO_2, Polyimide	~0.07	-	2300-25700		>4-5	158, 189-191

Table 1. Overview of nanocarbon-based microelectrode arrays (MEAs) and field-effect transistors (FETs).

* represents values obtained from the graphs or plots from the respective references.

Acknowledgements

T. Cohen-Karni would like to thank the National Science Foundation (CBET1552833), the Office of Naval Research (N000141712368).

Conflicts of interest

Sahil K. Rastogi, Anna Kalmykov, Nicholas Johnson and Tzahi Cohen-Karni declare that they have no conflicts of interest.

REFERENCES

1. E. R. Kandel, J. H. Schwartz, T. M. Jessell, S. A. Siegelbaum and A. J. Hudspeth, *Principles of neural science*, McGraw-hill New York, 2000.
2. B. F. Hoffman and P. F. Cranefield, *Electrophysiology of the Heart*, McGraw-Hill, Blakiston Division, 1960.
3. L. Galvani, *Bologna : Tip. Istituto delle Scienze*, 1791.
4. K. S. Cole and H. J. Curtis, *The Journal of general physiology*, 1939, **22**, 649-670.
5. A. L. Hodgkin and A. F. Huxley, *The Journal of physiology*, 1952, **117**, 500.
6. M. E. Josephson, *Clinical cardiac electrophysiology: techniques and interpretations*, Lippincott Williams & Wilkins, 2008.
7. P. Calabresi, N. Mercuri, G. Sancesario and G. Bernardi, *Brain: a journal of neurology*, 1993, **116**, 433-452.
8. D. Farwell and M. H. Gollob, *Canadian Journal of Cardiology*, 2007, **23**, 16A-22A.
9. H. N. Rubaiy, *Journal of Pharmacy & Pharmaceutical Sciences*, 2017, **20**, 48-67.
10. J. J. Clare, *Discovery medicine*, 2010, **9**, 253-260.
11. E. Freud, J. C. Culham, D. C. Plaut and M. Behrmann, *eLife*, 2017, **6**.
12. S. K. Rastogi and T. Cohen-Karni, in *Encyclopedia of Biomedical Engineering*, Elsevier, 2017.
13. M. Bove, M. Grattarola, S. Martinoia and G. Verreschi, *Bioelectrochemistry and bioenergetics*, 1995, **38**, 255-265.
14. M. E. Spira and A. Hai, *Nature nanotechnology*, 2013, **8**, 83-94.
15. N. Shmoel, N. Rabieh, S. M. Ojovan, H. Erez, E. Maydan and M. E. Spira, *Scientific reports*, 2016, **6**, 27110.
16. K. Woeppel, Q. Yang and X. T. Cui, *Current Opinion in Biomedical Engineering*, 2017.
17. S. M. Wellman, J. R. Eles, K. A. Ludwig, J. P. Seymour, N. J. Michelson, W. E. McFadden, A. L. Vazquez and T. D. Kozai, *Advanced functional materials*, 2018, **28**, 1701269.
18. H. A. Ledesma and B. Tian, *Journal of Materials Chemistry B*, 2017, **5**, 4276-4289.
19. T. Cohen-Karni, R. Langer and D. S. Kohane, *ACS nano*, 2012, **6**, 6541-6545.
20. M. F. De Volder, S. H. Tawfick, R. H. Baughman and A. J. Hart, *science*, 2013, **339**, 535-539.
21. L. Radushkevich and V. Lukyanovich, *J. Phys. Chem.(Moscow)*, 1952, **26**, 88-95.
22. S. Iijima, *nature*, 1991, **354**, 56.
23. S. Iijima and T. Ichihashi, *nature*, 1993, **363**, 603.
24. P. L. McEuen, M. S. Fuhrer and H. Park, *IEEE transactions on nanotechnology*, 2002, **99**, 78-85.
25. L. Bareket-Keren and Y. Hanein, *Frontiers in neural circuits*, 2013, **6**, 122.
26. A. Bianco, K. Kostarelos and M. Prato, *Current opinion in chemical biology*, 2005, **9**, 674-679.
27. J. Prasek, J. Drbohlavova, J. Chomoucka, J. Hubalek, O. Jasek, V. Adam and R. Kizek, *Journal of Materials Chemistry*, 2011, **21**, 15872-15884.
28. G. Hong, S. Diao, A. L. Antaris and H. Dai, *Chemical reviews*, 2015, **115**, 10816-10906.
29. P. Wick, P. Manser, L. K. Limbach, U. Dettlaff-Weglikowska, F. Krumeich, S. Roth, W. J. Stark and A. Bruinink, *Toxicology letters*, 2007, **168**, 121-131.

30. L.-C. Ong, F. F.-L. Chung, Y.-F. Tan and C.-O. Leong, *Archives of toxicology*, 2016, **90**, 103-118.
31. S. Vardharajula, S. Z. Ali, P. M. Tiwari, E. Eroğlu, K. Vig, V. A. Dennis and S. R. Singh, *International journal of nanomedicine*, 2012, **7**, 5361.
32. C. P. Firme and P. R. Bandaru, *Nanomedicine: Nanotechnology, Biology and Medicine*, 2010, **6**, 245-256.
33. C. M. Sayes, F. Liang, J. L. Hudson, J. Mendez, W. Guo, J. M. Beach, V. C. Moore, C. D. Doyle, J. L. West, W. E. Billups, K. D. Ausman and V. L. Colvin, *Toxicology letters*, 2006, **161**, 135-142.
34. V. Martinelli, G. Cellot, F. M. Toma, C. S. Long, J. H. Caldwell, L. Zentilin, M. Giacca, A. Turco, M. Prato, L. Ballerini and L. Mestroni, *ACS nano*, 2013, **7**, 5746-5756.
35. V. Martinelli, G. Cellot, F. M. Toma, C. S. Long, J. H. Caldwell, L. Zentilin, M. Giacca, A. Turco, M. Prato, L. Ballerini and L. Mestroni, *Nano letters*, 2012, **12**, 1831-1838.
36. G. Cellot, E. Cilia, S. Cipollone, V. Rancic, A. Sucapane, S. Giordani, L. Gambazzi, H. Markram, M. Grandolfo, D. Scaini, F. Gelain, L. Casalis, M. Prato, M. Giugliano and L. Ballerini, *Nature nanotechnology*, 2009, **4**, 126.
37. S. Usmani, E. R. Aurand, M. Medelin, A. Fabbro, D. Scaini, J. Laishram, F. B. Rosselli, A. Ansuini, D. Zoccolan, M. Scarselli, M. De Crescenzi, S. Bosi, M. Prato and L. Ballerini, *Science advances*, 2016, **2**, e1600087.
38. M. P. Mattson, R. C. Haddon and A. M. Rao, *Journal of Molecular Neuroscience*, 2000, **14**, 175-182.
39. H. Hu, Y. Ni, V. Montana, R. C. Haddon and V. Parpura, *Nano letters*, 2004, **4**, 507-511.
40. H. Hu, Y. Ni, S. K. Mandal, V. Montana, B. Zhao, R. C. Haddon and V. Parpura, *The Journal of Physical Chemistry B*, 2005, **109**, 4285-4289.
41. M. Mattioli-Belmonte, G. Vozzi, Y. Whulanza, M. Seggiani, V. Fantauzzi, G. Orsini and A. Ahluwalia, *Materials Science and Engineering: C*, 2012, **32**, 152-159.
42. M. David-Pur, L. Bareket-Keren, G. Beit-Yaakov, D. Raz-Prag and Y. Hanein, *Biomedical microdevices*, 2014, **16**, 43-53.
43. K. Wang, H. A. Fishman, H. Dai and J. S. Harris, *Nano letters*, 2006, **6**, 2043-2048.
44. T. Gabay, M. Ben-David, I. Kalifa, R. Sorkin, Z. R. Abrams, E. Ben-Jacob and Y. Hanein, *Nanotechnology*, 2007, **18**, 035201.
45. M. K. Gheith, T. C. Pappas, A. V. Liopo, V. A. Sinani, B. S. Shim, M. Motamedi, J. P. Wicksted and N. A. Kotov, *Advanced Materials*, 2006, **18**, 2975-2979.
46. A. Mazzatenta, M. Giugliano, S. Campidelli, L. Gambazzi, L. Businaro, H. Markram, M. Prato and L. Ballerini, *Journal of Neuroscience*, 2007, **27**, 6931-6936.
47. Z. Yu, T. E. McKnight, M. N. Ericson, A. V. Melechko, M. L. Simpson and B. Morrison, *Nano letters*, 2007, **7**, 2188-2195.
48. S. Park, P. Dong-Won, C.-S. Yang, K.-R. Kim, J.-H. Kwak, H.-M. So, C. W. Ahn, B. S. Kim, H. Chang and J.-O. Lee, *ACS nano*, 2011, **5**, 7061-7068.
49. D. W. Jeong, J. Jung, G. H. Kim, C.-S. Yang, J. J. Kim, S. D. Jung and J.-O. Lee, *Nanotechnology*, 2015, **26**, 335701.
50. D. W. Jeong, G. H. Kim, N. Y. Kim, Z. Lee, S. D. Jung and J.-O. Lee, *RSC Advances*, 2017, **7**, 3273-3281.
51. C. Nick, R. Joshi, J. J. Schneider and C. Thielemann, *Biointerphases*, 2012, **7**, 58.
52. E. W. Keefer, B. R. Botterman, M. I. Romero, A. F. Rossi and G. W. Gross, *Nature nanotechnology*, 2008, **3**, 434-439.

53. Y.-C. Chen, H.-L. Hsu, Y.-T. Lee, H.-C. Su, S.-J. Yen, C.-H. Chen, W.-L. Hsu, T.-R. Yew, S.-R. Yeh and D.-J. Yao, *Journal of neural engineering*, 2011, **8**, 034001.
54. J. Zhang, X. Liu, W. Xu, W. Luo, M. Li, F. Chu, L. Xu, A. Cao, J. Guan, S. Tang and X. Duan, *Nano letters*, 2018, **18**, 2903-2911.
55. B. Vigolo, A. Penicaud, C. Coulon, C. Sauder, R. Pailler, C. Journet, P. Bernier and P. Poulin, *Science*, 2000, **290**, 1331-1334.
56. L. M. Ericson, H. Fan, H. Peng, V. A. Davis, W. Zhou, J. Sulpizio, Y. Wang, R. Booker, J. Vavro, C. Guthy, A. N. G. Parra-Vasquez, M. J. Kim, S. Ramesh, R. K. Saini, C. Kittrell, G. Lavin, H. Schmidt, W. W. Adams, W. E. Billups, M. Pasquali, W.-F. Hwang, R. H. Hauge, J. E. Fischer and R. E. Smalley, *Science*, 2004, **305**, 1447-1450.
57. N. Behabtu, C. C. Young, D. E. Tsentalovich, O. Kleinerman, X. Wang, A. W. Ma, E. A. Bengio, R. F. ter Waarbeek, J. J. de Jong, R. E. Hoogerwerf, S. B. Fairchild, J. B. Ferguson, B. Maruyama, J. Kono, Y. Talmon, Y. Cohen, M. J. Otto and M. Pasquali, *science*, 2013, **339**, 182-186.
58. F. Vitale, S. R. Summerson, B. Aazhang, C. Kemere and M. Pasquali, *ACS nano*, 2015, **9**, 4465-4474.
59. F. Vitale, D. Vercosa, A. V. Rodriguez, S. S. Pamulapati, F. Seibt, E. Lewis, J. S. Yan, K. Badhiwala, M. Adnan, G. Royer-Carfagni, M. Beielein, C. Kemere, M. Pasquali and J. T. Robinson, *Nano letters*, 2017.
60. O. A. Williams, *Diamond and Related Materials*, 2011, **20**, 621-640.
61. O. A. Williams, M. Nesladek, M. Daenen, S. Michaelson, A. Hoffman, E. Osawa, K. Haenen and R. B. Jackman, *Diamond and Related Materials*, 2008, **17**, 1080-1088.
62. D. M. Gruen, *Annual Review of Materials Science*, 1999, **29**, 211-259.
63. G. M. Swain, A. B. Anderson and J. C. Angus, *MRS Bulletin*, 1998, **23**, 56-60.
64. J. E. Field, *The properties of diamond*, Academic Press, 1979.
65. B. V. Deryagin and D. V. Fedoseev, *Russian Chemical Reviews*, 1970, **39**, 783-788.
66. J. C. Angus, H. A. Will and W. S. Stanko, *Journal of Applied Physics*, 1968, **39**, 2915-2922.
67. D. J. Poferl, N. C. Gardner and J. C. Angus, *Journal of Applied Physics*, 1973, **44**, 1428-1434.
68. J. C. Angus and C. C. Hayman, *Science (New York, N.Y.)*, 1988, **241**, 913-921.
69. W. A. Yarbrough and R. Messier, *Science*, 1990, **247**, 688-696.
70. P. W. May, *Philosophical Transactions of the Royal Society A: Mathematical, Physical and Engineering Sciences*, 2000, **358**, 473-495.
71. S. Matsumoto, Y. Sato, M. Tsutsumi and N. Setaka, *Journal of Materials Science*, 1982, **17**, 3106-3112.
72. R. Haubner and B. Lux, *Diamond and Related Materials*, 1993, **2**, 1277-1294.
73. T. Kawato and K.-i. Kondo, *Japanese journal of applied physics*, 1987, **26**, 1429.
74. Y. Hirose and Y. Terasawa, *Japanese journal of applied physics*, 1986, **25**, L519.
75. B. Singh, Y. Arie, A. Levine and O. Mesker, *Applied physics letters*, 1988, **52**, 451-452.
76. J. Philip, P. Hess, T. Feygelson, J. E. Butler, S. Chattopadhyay, K. H. Chen and L. C. Chen, *Journal of Applied Physics*, 2003, **93**, 2164-2171.
77. O. Matsumoto and T. Katagiri, *Thin Solid Films*, 1987, **146**, 283-289.
78. O. Matsumoto, H. Toshima and Y. Kanzaki, *Thin Solid Films*, 1985, **128**, 341-351.
79. Y. Saito, S. Matsuda and S. Nogita, *Journal of materials science letters*, 1986, **5**, 565-568.

80. A. Sawabe and T. Inuzuka, *Thin Solid Films*, 1986, **137**, 89-99.
81. A. Sawabe and T. Inuzuka, *Applied Physics Letters*, 1985, **46**, 146-147.
82. K. Suzuki, A. Sawabe, H. Yasuda and T. Inuzuka, *Applied Physics Letters*, 1987, **50**, 728-729.
83. K. Kurihara, K. Sasaki, M. Kawarada and N. Koshino, *Applied physics letters*, 1988, **52**, 437-438.
84. L. Hanssen, W. Carrington, J. Butler and K. Snail, *Materials Letters*, 1988, **7**, 289-292.
85. L. Tang, C. Tsai, W. W. Gerberich, L. Kruckeberg and D. R. Kania, *Biomaterials*, 1995, **16**, 483-488.
86. P. W. May, E. M. Regan, A. Taylor, J. Uney, A. D. Dick and J. McGeehan, *Diamond and related materials*, 2012, **23**, 100-104.
87. P. Ariano, P. Baldelli, E. Carbone, A. Gilardino, A. Lo Giudice, D. Lovisolo, C. Manfredotti, M. Novara, H. Sternschulte and E. Vittone, *Diamond and Related Materials*, 2005, **14**, 669-674.
88. M. Kalbacova, A. Broz, O. Babchenko and A. Kromka, *physica status solidi (b)*, 2009, **246**, 2774-2777.
89. M. Kalbacova, B. Rezek, V. Baresova, C. Wolf-Brandstetter and A. Kromka, *Acta Biomaterialia*, 2009, **5**, 3076-3085.
90. M. Amaral, P. S. Gomes, M. A. Lopes, J. D. Santos, R. F. Silva and M. H. Fernandes, *Acta biomaterialia*, 2009, **5**, 755-763.
91. Y.-C. Chen, D.-C. Lee, C.-Y. Hsiao, Y.-F. Chung, H.-C. Chen, J. P. Thomas, W.-F. Pong, N.-H. Tai, I. N. Lin and I.-M. Chiu, *Biomaterials*, 2009, **30**, 3428-3435.
92. Y.-C. Chen, D.-C. Lee, T.-Y. Tsai, C.-Y. Hsiao, J.-W. Liu, C.-Y. Kao, H.-K. Lin, H.-C. Chen, T. J. Palathinkal, W.-F. Pong, N.-H. Tai, I. N. Lin and I.-M. Chiu, *Biomaterials*, 2010, **31**, 5575-5587.
93. W. C. Clem, S. Chowdhury, S. A. Catledge, J. J. Weimer, F. M. Shaikh, K. M. Hennessy, V. V. Konovalov, M. R. Hill, A. Waterfeld, S. L. Bellis and Y. K. Vohra, *Biomaterials*, 2008, **29**, 3461-3468.
94. C. G. Specht, O. A. Williams, R. B. Jackman and R. Schoepfer, *Biomaterials*, 2004, **25**, 4073-4078.
95. A. Thalhammer, R. J. Edgington, L. A. Cingolani, R. Schoepfer and R. B. Jackman, *Biomaterials*, 2010, **31**, 2097-2104.
96. A. Bendali, C. Agnès, S. Meffert, V. Forster, A. Bongrain, J.-C. Arnault, J.-A. Sahel, A. Offenhäusser, P. Bergonzo and S. Picaud, *PLoS ONE*, 2014, **9**, e92562.
97. A. C. Taylor, B. Vagaska, R. Edgington, C. Hébert, P. Ferretti, P. Bergonzo and R. B. Jackman, *Journal of Neural Engineering*, 2015, **12**, 066016.
98. Y. V. Pelskov, A. Y. Sakharova, M. D. Krotova, L. L. Bouilov and B. V. Spitsyn, *Journal of Electroanalytical Chemistry and Interfacial Electrochemistry*, 1987, **228**, 19-27.
99. V. Carabelli, A. Marcantoni, F. Picollo, A. Battiato, E. Bernardi, A. Pasquarelli, P. Olivero and E. Carbone, *ACS Chemical Neuroscience*, 2017, **8**, 252-264.
100. S. Wenmackers, V. Vermeeren, M. Vandeven, M. Ameloot, N. Bijnens, K. Haenen, L. Michiels and P. Wagner, *physica status solidi (a)*, 2009, **206**, 391-408.
101. V. Vermeeren, S. Wenmackers, P. Wagner and L. Michiels, *Sensors*, 2009, **9**, 5600-5636.
102. J. Lee and S.-M. Park, *Analytica Chimica Acta*, 2005, **545**, 27-32.

103. E. Popa, H. Notsu, T. Miwa, D. A. Tryk and A. Fujishima, *Electrochemical and solid-state letters*, 1999, **2**, 49-51.
104. E. Popa, Y. Kubota, D. A. Tryk and A. Fujishima, *Analytical chemistry*, 2000, **72**, 1724-1727.
105. J. M. Halpern, S. Xie, G. P. Sutton, B. T. Higashikubo, C. A. Chestek, H. Lu, H. J. Chiel and H. B. Martin, *Diamond and Related Materials*, 2006, **15**, 183-187.
106. F. Vahidpour, L. Curley, I. Biró, M. McDonald, D. Croux, P. Pobedinskas, K. Haenen, M. Giugliano, Z. V. Živcová, L. Kavan and M. Nesládek, *physica status solidi (a)*, 2016, **214**, 1532347-1532347.
107. V. Maybeck, R. Edgington, A. Bongrain, J. O. Welch, E. Scorsone, P. Bergonzo, R. B. Jackman, A. Offenhäusser, *Advanced Healthcare Materials*, 2013, **3**, 283-289.
108. G. Piret, C. Hébert, J.-P. Mazellier, L. Rousseau, E. Scorsone, M. Cottance, G. Lissorgues, M. O. Heuschkel, S. Picaud, P. Bergonzo and B. Yvert, *Biomaterials*, 2015, **53**, 173-183.
109. M. Dankerl, S. Eick, B. Hofmann, M. Hauf, S. Ingebrandt, A. Offenhäusser, M. Stutzmann and J. A. Garrido, *Advanced Functional Materials*, 2009, **19**, 2915-2923.
110. J. M. Halpern, M. J. Cullins, H. J. Chiel and H. B. Martin, *Diamond and Related Materials*, 2010, **19**, 178-181.
111. P. Ariano, A. Lo Giudice, A. Marcantoni, E. Vittone, E. Carbone and D. Lovisolo, *Biosensors and Bioelectronics*, 2009, **24**, 2046-2050.
112. P. Bergonzo, A. Bongrain, E. Scorsone, A. Bendali, L. Rousseau, G. Lissorgues, P. Mailley, Y. Li, T. Kauffmann, F. Goy, B. Yvert, J. A. Sahel and S. Picaud, *IRBM*, 2011, **32**, 91-94.
113. A. E. Hadjinicolaou, R. T. Leung, D. J. Garrett, K. Ganesan, K. Fox, D. A. X. Nayagam, M. N. Shivdasani, H. Meffin, M. R. Ibbotson, S. Prawer and B. J. O'Brien, *Biomaterials*, 2012, **33**, 5812-5820.
114. D. J. Garrett, K. Ganesan, A. Stacey, K. Fox, H. Meffin and S. Prawer, *Journal of Neural Engineering*, 2012, **9**, 016002.
115. Y. Cai, F. Edin, Z. Jin, A. Alexsson, O. Gudjonsson, W. Liu, H. Rask-Andersen, M. Karlsson and H. Li, *Acta Biomaterialia*, 2016, **31**, 211-220.
116. K. S. Novoselov, A. K. Geim, S. V. Morozov, D. Jiang, Y. Zhang, S. V. Dubonos, I. V. Grigorieva and A. A. Firsov, *science*, 2004, **306**, 666-669.
117. A. K. Geim, *science*, 2009, **324**, 1530-1534.
118. K. V. Emtsev, A. Bostwick, K. Horn, J. Jobst, G. L. Kellogg, L. Ley, J. L. McChesney, T. Ohta, S. A. Reshanov, J. Röhrl, E. Rotenberg, A. K. Schmid, D. Waldmann, H. B. Weber and T. Seyller, *Nature materials*, 2009, **8**, 203-207.
119. K. S. Kim, Y. Zhao, H. Jang, S. Y. Lee, J. M. Kim, K. S. Kim, J.-H. Ahn, P. Kim, J.-Y. Choi and B. H. Hong, *nature*, 2009, **457**, 706-710.
120. D. Li, M. B. Müller, S. Gilje, R. B. Kaner and G. G. Wallace, *Nature nanotechnology*, 2008, **3**, 101-105.
121. S. K. Rastogi, J. Bliley, G. Raghavan, D. J. Shiwarski, A. W. Feinberg and T. Cohen-Karni, *Cellular and Molecular Bioengineering* 2018.
122. R. Garg, S. K. Rastogi, M. Lamparski, S. C. de la Barrera, G. T. Pace, N. T. Nuhfer, B. M. Hunt, V. Meunier and T. Cohen-Karni, *ACS nano*, 2017, **11**, 6301-6311.
123. S. K. Rastogi, G. Raghavan, G. Yang and T. Cohen-Karni, *Nano Letters*, 2017, **17**, 3297-3301.

124. G. Eda, G. Fanchini and M. Chhowalla, *Nature nanotechnology*, 2008, **3**, 270-274.
125. S. Park and R. S. Ruoff, *Nature nanotechnology*, 2009, **4**, 217-224.
126. C. Berger, Z. Song, X. Li, X. Wu, N. Brown, C. Naud, D. Mayou, T. Li, J. Hass, A. N. Marchenkov, E. H. Conrad, P. N. First and W. A. de Heer, *Science*, 2006, **312**, 1191-1196.
127. X. Li, W. Cai, J. An, S. Kim, J. Nah, D. Yang, R. Piner, A. Velamakanni, I. Jung, E. Tutuc, S. K. Banerjee, L. Colombo and R. S. Ruoff, *Science*, 2009, **324**, 1312-1314.
128. C. Mattevi, H. Kim and M. Chhowalla, *Journal of Materials Chemistry*, 2011, **21**, 3324-3334.
129. J. W. Suk, A. Kitt, C. W. Magnuson, Y. Hao, S. Ahmed, J. An, A. K. Swan, B. B. Goldberg and R. S. Ruoff, *ACS nano*, 2011, **5**, 6916-6924.
130. X. Liang, B. A. Sperling, I. Calizo, G. Cheng, C. A. Hacker, Q. Zhang, Y. Obeng, K. Yan, H. Peng, Q. Li, X. Zhu, H. Yuan, A. R. H. Walker, Z. Liu, L.-M. Peng and C. A. Richter, *ACS nano*, 2011, **5**, 9144-9153.
131. E. H. Lock, M. Baraket, M. Laskoski, S. P. Mulvaney, W. K. Lee, P. E. Sheehan, D. R. Hines, J. T. Robinson, J. Tosado, M. S. Fuhrer, S. C. Hernández and S. G. Walton, *Nano letters*, 2011, **12**, 102-107.
132. A. M. Pinto, I. C. Gonçalves and F. D. Magalhães, *Colloids and Surfaces B: Biointerfaces*, 2013, **111**, 188-202.
133. Y. Zhang, T. R. Nayak, H. Hong and W. Cai, *Nanoscale*, 2012, **4**, 3833-3842.
134. K.-H. Liao, Y.-S. Lin, C. W. Macosko and C. L. Haynes, *ACS applied materials & interfaces*, 2011, **3**, 2607-2615.
135. Y. Zhang, S. F. Ali, E. Dervishi, Y. Xu, Z. Li, D. Casciano and A. S. Biris, *Acs Nano*, 2010, **4**, 3181-3186.
136. A. Sasidharan, L. Panchakarla, P. Chandran, D. Menon, S. Nair, C. Rao and M. Koyakutty, *Nanoscale*, 2011, **3**, 2461-2464.
137. A. Sasidharan, L. S. Panchakarla, A. R. Sadanandan, A. Ashokan, P. Chandran, C. M. Girish, D. Menon, S. V. Nair, C. Rao and M. Koyakutty, *Small*, 2012, **8**, 1251-1263.
138. W. Hu, C. Peng, M. Lv, X. Li, Y. Zhang, N. Chen, C. Fan and Q. Huang, *Acs Nano*, 2011, **5**, 3693-3700.
139. S.-R. Ryoo, Y.-K. Kim, M.-H. Kim and D.-H. Min, *Acs Nano*, 2010, **4**, 6587-6598.
140. M. Kalbacova, A. Broz, J. Kong and M. Kalbac, *Carbon*, 2010, **48**, 4323-4329.
141. O. N. Ruiz, K. S. Fernando, B. Wang, N. A. Brown, P. G. Luo, N. D. McNamara, M. Vangsness, Y.-P. Sun and C. E. Bunker, *Acs Nano*, 2011, **5**, 8100-8107.
142. S. Y. Park, J. Park, S. H. Sim, M. G. Sung, K. S. Kim, B. H. Hong and S. Hong, *Advanced Materials*, 2011, **23**.
143. N. Li, Q. Zhang, S. Gao, Q. Song, R. Huang, L. Wang, L. Liu, J. Dai, M. Tang and G. Cheng, *Scientific reports*, 2013, **3**, 1604.
144. N. Li, X. Zhang, Q. Song, R. Su, Q. Zhang, T. Kong, L. Liu, G. Jin, M. Tang and G. Cheng, *Biomaterials*, 2011, **32**, 9374-9382.
145. V. C. Sanchez, A. Jachak, R. H. Hurt and A. B. Kane, *Chemical research in toxicology*, 2012, **25**, 15-34.
146. S. W. Perry, J. P. Norman, J. Barbieri, E. B. Brown and H. A. Gelbard, *Biotechniques*, 2011, **50**, 98-115.
147. M. Karbowski and R. Youle, *Cell Death & Differentiation*, 2003, **10**, 870-880.
148. G. Kroemer, G. Mariño and B. Levine, *Molecular cell*, 2010, **40**, 280-293.

149. N. Mizushima, T. Yoshimori and B. Levine, *Cell*, 2010, **140**, 313-326.
150. S. Kimura, T. Noda and T. Yoshimori, *Autophagy*, 2007, **3**, 452-460.
151. K. Deisseroth, *Nature methods*, 2011, **8**, 26-29.
152. D.-W. Park, A. A. Schendel, S. Mikael, S. K. Brodnick, T. J. Richner, J. P. Ness, M. R. Hayat, F. Atry, S. T. Frye, R. Pashaie, S. Thongpang, Z. Ma and J. C. Williams, *Nature Communications*, 2014, **5**.
153. J. Duranteau, N. S. Chandel, A. Kulisz, Z. Shao and P. T. Schumacker, *Journal of biological chemistry*, 1998, **273**, 11619-11624.
154. S. Huang, A. A. Heikal and W. W. Webb, *Biophysical journal*, 2002, **82**, 2811-2825.
155. F. C. Pascut, H. T. Goh, N. Welch, L. D. Buttery, C. Denning and I. Notingher, *Biophysical journal*, 2011, **100**, 251-259.
156. G. W. Gross, W. Y. Wen and J. W. Lin, *Journal of neuroscience methods*, 1985, **15**, 243-252.
157. Y. Qiang, K. J. Seo, X. Zhao, P. Artoni, N. H. Golshan, S. Culaclii, P. M. Wang, W. Liu, K. S. Ziemer, M. Fagiolini and H. Fang, *Advanced Functional Materials*, 2017, **27**.
158. T. Cohen-Karni, Q. Qing, Q. Li, Y. Fang and C. M. Lieber, *Nano letters*, 2010, **10**, 1098-1102.
159. L. H. Hess, M. Jansen, V. Maybeck, M. V. Hauf, M. Seifert, M. Stutzmann, I. D. Sharp, A. Offenhäusser and J. A. Garrido, *Advanced Materials*, 2011, **23**, 5045-5049.
160. Z. Cheng, J. Hou, Q. Zhou, T. Li, H. Li, L. Yang, K. Jiang, C. Wang, Y. Li and Y. Fang, *Nano letters*, 2013, **13**, 2902-2907.
161. D. Kuzum, H. Takano, E. Shim, J. C. Reed, H. Juul, A. G. Richardson, J. de Vries, H. Bink, M. A. Dichter, T. H. Lucas, D. A. Coulter, E. Cubukcu and B. Litt, *Nature communications*, 2014, **5**.
162. D. Kireev, S. Seyock, M. Ernst, V. Maybeck, B. Wolfrum and A. Offenhäusser, *Biosensors*, 2017, **7**, 1.
163. Y. Xu, K. Sheng, C. Li and G. Shi, *ACS nano*, 2010, **4**, 4324-4330.
164. W. Chen and L. Yan, *Nanoscale*, 2011, **3**, 3132-3137.
165. B. G. Choi, M. Yang, W. H. Hong, J. W. Choi and Y. S. Huh, *ACS nano*, 2012, **6**, 4020-4028.
166. J. Lin, Z. Peng, Y. Liu, F. Ruiz-Zepeda, R. Ye, E. L. Samuel, M. J. Yacaman, B. I. Yakobson and J. M. Tour, *Nature communications*, 2014, **5**, 5714.
167. N. Li, Q. Zhang, S. Gao, Q. Song, R. Huang, L. Wang, L. Liu, J. Dai, M. Tang and G. Cheng, *Scientific reports*, 2013, **3**, 1604.
168. S. W. Crowder, D. Prasai, R. Rath, D. A. Balikov, H. Bae, K. I. Bolotin and H.-J. Sung, *Nanoscale*, 2013, **5**, 4171-4176.
169. X. Dong, X. Wang, L. Wang, H. Song, H. Zhang, W. Huang and P. Chen, *ACS applied materials & interfaces*, 2012, **4**, 3129-3133.
170. X. Feng, Y. Zhang, J. Zhou, Y. Li, S. Chen, L. Zhang, Y. Ma, L. Wang and X. Yan, *Nanoscale*, 2015, **7**, 2427-2432.
171. B. Yu, D. Kuang, S. Liu, C. Liu and T. Zhang, *Sensors and Actuators B: Chemical*, 2014, **205**, 120-126.
172. Y. Ma, M. Zhao, B. Cai, W. Wang, Z. Ye and J. Huang, *Biosensors and Bioelectronics*, 2014, **59**, 384-388.

173. H. Y. Yue, S. Huang, J. Chang, C. Heo, F. Yao, S. Adhikari, F. Gunes, L. C. Liu, T. H. Lee, E. S. Oh, B. Li, J. J. Zhang, T. Q. Huy, N. Van Luan and Y. H. Lee, *ACS nano*, 2014, **8**, 1639-1646.
174. X.-C. Dong, H. Xu, X.-W. Wang, Y.-X. Huang, M. B. Chan-Park, H. Zhang, L.-H. Wang, W. Huang and P. Chen, *ACS nano*, 2012, **6**, 3206-3213.
175. M. Zhou, Y. Zhai and S. Dong, *Analytical chemistry*, 2009, **81**, 5603-5613.
176. D. Du, Z. Zou, Y. Shin, J. Wang, H. Wu, M. H. Engelhard, J. Liu, I. A. Aksay and Y. Lin, *Analytical Chemistry*, 2010, **82**, 2989-2995.
177. S. K. Ameri, P. Singh, R. D'Angelo, W. Stoppel, L. Black and S. R. Sonkusale, *Engineering in Medicine and Biology Society (EMBC), 2016 IEEE 38th Annual International Conference of the*. IEEE, 2016.
178. Y. Lu, H. Lyu, A. G. Richardson, T. H. Lucas and D. Kuzum, *Scientific reports*, 2016, **6**, 33526.
179. L. Chen, L. Guo, Y. Wu, Y. Jia, Z. Li and X. Chen, *RSC Advances*, 2013, **3**, 13926-13933.
180. S. Zheng, Z. Li, Z.-S. Wu, Y. Dong, F. Zhou, S. Wang, Q. Fu, C. Sun, L. Guo and X. Bao, *ACS nano*, 2017, **11**, 4009-4016.
181. C. Yang, H. Bi, D. Wan, F. Huang, X. Xie and M. Jiang, *Journal of Materials Chemistry A*, 2013, **1**, 770-775.
182. M. Hiramatsu and M. Hori, *Carbon nanowalls: synthesis and emerging applications*, Springer Science & Business Media, 2010.
183. K. Yu, Z. Bo, G. Lu, S. Mao, S. Cui, Y. Zhu, X. Chen, R. S. Ruoff and J. Chen, *Nanoscale research letters*, 2011, **6**, 202.
184. O. Akhavan and E. Ghaderi, *ACS nano*, 2010, **4**, 5731-5736.
185. R. Ion, S. Vizireanu, C. E. Stancu, C. Luculescu, A. Cimpean and G. Dinescu, *Materials Science and Engineering: C*, 2015, **48**, 118-125.
186. R. Ion, S. Vizireanu, C. Luculescu, A. Cimpean and G. Dinescu, *Journal of Physics D: Applied Physics*, 2016, **49**, 274004.
187. S. Mao, K. Yu, J. Chang, D. A. Steeber, L. E. Ocola and J. Chen, *Scientific reports*, 2013, **3**, 1696.
188. N. Collaert, C. M. Lopez, D. J. Cott, J. Cools, D. Braeken and M. De Volder, *Carbon*, 2014, **67**, 178-184.
189. B. P. Timko, T. Cohen-Karni, G. Yu, Q. Qing, B. Tian and C. M. Lieber, *Nano letters*, 2009, **9**, 914-918.
190. T. Cohen-Karni, D. Casanova, J. F. Cahoon, Q. Qing, D. C. Bell and C. M. Lieber, *Nano letters*, 2012, **12**, 2639-2644.
191. T. Cohen-Karni, B. P. Timko, L. E. Weiss and C. M. Lieber, *Proceedings of the National Academy of Sciences*, 2009, **106**, 7309-7313.